

Imaging the coherent propagation of collective modes in the excitonic insulator candidate Ta_2NiSe_5 at room temperature

Paolo Andrich,^{1,*} Hope M. Bretscher,^{1,*} Yuta Murakami,² Denis Golež,²
Benjamin Remez,¹ Prachi Telang,³ Anupam Singh,³ Luminita Harnagea,³ Nigel R.
Cooper,¹ Andrew J. Millis,^{2,4} Philipp Werner,⁵ A. K. Sood,⁶ and Akshay Rao¹

¹*Cavendish Laboratory, University of Cambridge, Cambridge CB3 0HE, United Kingdom*

²*Center for Computational Quantum Physics, Flatiron Institute, New York, New York 10010, USA*

³*Department of Physics, Indian Institute of Science Education and Research, Pune, Maharashtra 411008, India*

⁴*Department of Physics, Columbia University, New York, New York 10027, USA*

⁵*Department of Physics, University of Fribourg, Fribourg 1700, Switzerland*

⁶*Department of Physics, Indian Institute of Science, Bangalore, Karnataka 560012, India*

(Dated: August 29, 2021)

Excitonic insulating (EI) materials are predicted to host a condensate of electron-hole pairs in their ground state, giving rise to collective many-body effects. Although several bulk materials have been proposed as EIs recently, a direct observation of the characteristic collective behavior is still missing. Here, we use ultrafast, spatially-resolved, pump-probe microscopy to investigate the propagation of photoinduced excitations in a proposed EI, Ta_2NiSe_5 . Below the critical temperature for the EI phase (328 K), we observe the propagation, for distances of up to $1\ \mu\text{m}$, of coherent oscillatory modes in the THz range at velocities of the order of $10^5\ \text{m/s}$. We develop a theoretical framework to explain these findings and suggest that this behavior results from the hybridization of phonon modes with the phase mode of the EI. We infer that the ordered EI phase is driven predominantly by interorbital Coulomb interactions and that this system falls into the BCS-BEC crossover regime. This study provides a route for the investigation of collective properties in strongly correlated materials and paves the way for applications that can take advantage of these quantum phenomena up to room temperature.

In recent decades, considerable effort has been devoted to understanding and controlling macroscopic quantum states of matter, such as superconductivity and superfluidity. These exotic effects manifest themselves as the result of the collective behavior of the constituent particles and occur in systems as diverse as metals [1], cold-atoms [2], and exciton-polaritons [3]. These macroscopic condensates are generally accompanied by characteristic collective excitations, including the amplitude (Higgs) and the phase (Goldstone) modes [4–8]

Another important example of fermion pair condensation is the excitonic insulating (EI) phase, a state of matter that was first proposed more than 50 years ago [9–11]. It was theorized that, below a critical temperature (T_c), weakly screened Coulomb interactions in small bandgap semiconductors and semimetals could lead to the spontaneous formation of an exciton condensate, Fig. 1A. In the proposed theoretical framework, the condensate formation would result from the breaking of a $U(1)$ continuous symmetry existing in the “normal” phase, which describes the separate conservation of charges in the valence and conduction bands. This happens without explicitly affecting the symmetry of the Hamiltonian, meaning it is a spontaneous symmetry breaking, which in turn results in a gapless phase mode for the condensate [12]. Such a condensate could sustain collective excitations, resulting in quantum phenomena being apparent on macroscopic length-scales and, in principle, could manifest superfluid transport.

While an engineered EI phase has been realized at cryogenic temperatures in bilayer architectures [13–17]

and novel topological insulators [18], its discovery in a bulk material has been elusive for decades. Nevertheless, some transition metal chalcogenide (TMC) compounds have recently attracted interest as promising EI candidates [16, 17, 19–23]. The reduced dimensionality of TMCs results in a weak screening of the Coulomb interaction and large exciton binding energies. This could lead to condensation at non-cryogenic temperatures, which makes these systems unique platforms for the study of collective emergent properties.

Among this family of materials, particular attention has been devoted to Ta_2NiSe_5 following hints of the existence of an ordered, EI phase below $\simeq 328\ \text{K}$ [19–21, 24, 25]. This material is especially promising as a result of its quasi-1D structure (see Fig. 1A), where alternating chains of Ta and Ni atoms independently host conduction and valence band states [19]. The resulting physical separation between electrons and holes mirrors the conditions existing in bilayer systems and helps to stabilize the excitonic state. Experimental indications of the EI phase have been obtained, for instance, using equilibrium [19, 23] and time-resolved [20, 26], angle-resolved photoemission spectroscopy (ARPES), by analyzing the effect of physical and chemical pressure [25], and by detecting anomalies in the temperature dependence of transport [25] and phonon properties [21, 27] of the material. Despite various indications, we are still lacking a direct observation of the collective motion expected in the EI phase in this or other systems.

Contrary to the idealized situation described above, in real condensed matter systems the Coulomb attrac-

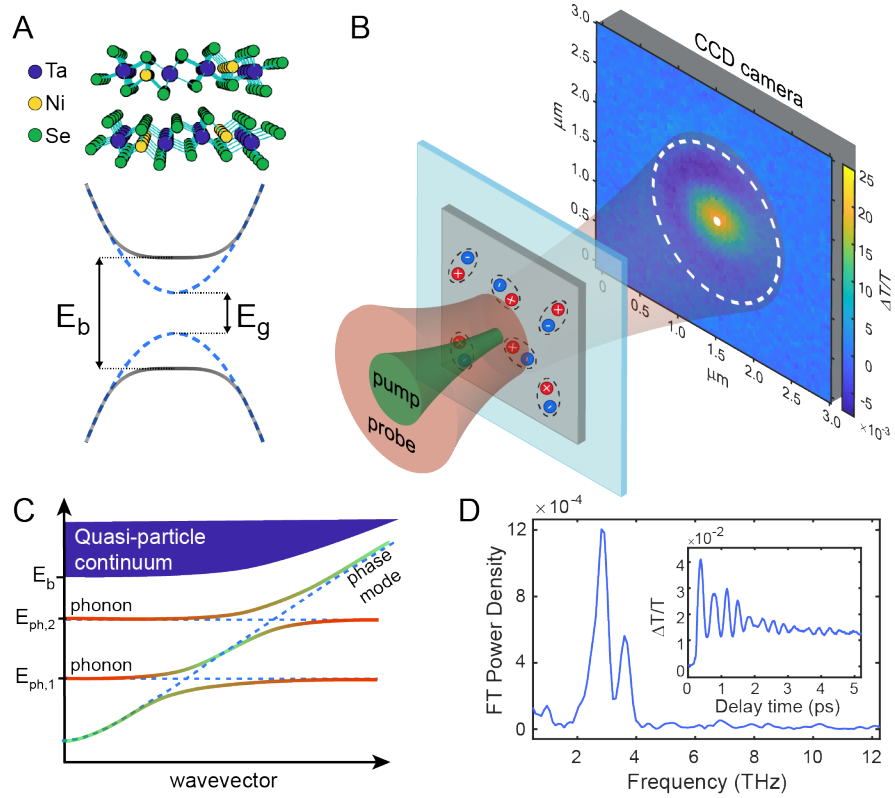


Figure 1. (A, top) Crystal structure of Ta_2NiSe_5 where the alignment of the atoms along one-dimensional chains is apparent. (A, bottom) Schematic electronic band structure for a prototypical excitonic insulator. Above the critical temperature the material is close to the semiconductor-semimetal transition (portrayed here as a semiconductor of energy gap E_g). Below the critical temperature, the exciton binding energy (E_b) exceeds the single-particle gap (E_g), resulting in a macroscopic coherent state. (B) Schematic of the measurement setup at the location of the sample with the photoinduced transmissivity change ($\Delta T/T$) signal). The white dot and dashed circle are examples of pixel regions over which we average the signal in our analysis. (C) Schematic diagram of a possible low-energy excitation structure for an excitonic insulator in the presence of electron-phonon coupling. The phonon modes of the material hybridize with the phase mode resulting in mixed phonon-phase modes as long as the energy gap in the phase mode dispersion at $k = 0$ is smaller than the phonon energy $E_{ph,i}$. The phonon and phase content of the modes is represented as a color gradient from green (pure phase mode) to red (pure phonon mode). (D) Photoinduced transmissivity change ($\Delta T/T$) as a function of the pump-probe delay time collected at the center of the pump region (inset) and its Fourier Transform power density.

tion is not the only relevant interaction, and there could exist coupling terms that explicitly modify the Hamiltonian's symmetry. Such a situation can emerge when electrons couple with phonons. In this case, the Hamiltonian's symmetry can be reduced to a discrete symmetry and the ordered, EI phase can be cooperatively driven by both the electron-phonon (el-ph) coupling and the Coulomb interaction [28]. An analogous situation occurs in the presence of hybridization between the conduction and valence bands [29, 30]. The presence of either of these scenarios can profoundly affect the properties of the collective modes in the ordered phase, and, for instance, would open a gap at $k \simeq 0$ in the dispersion of the phase mode, resulting in the suppression of proposed supertransport properties [31]. Therefore, it is crucial to understand to what extent these interactions drive the formation of the ordered phase and how this manifests in macroscopic material properties, such as transport and

real-space dynamics. A direct observation of the collective modes in the ordered phase would provide important insight into these questions.

Here, we probe the spatio-temporal dynamics of Ta_2NiSe_5 following photoexcitation using a recently developed femtosecond optical pump-probe microscopy technique [32], which provides sub 10 fs time-resolution and 10 nm spatial precision [33, 34] (see Fig. 1B). At room temperature ($< T_c$), we observe the presence of an oscillatory response at frequencies close to the expected phonon modes of the crystal [21]. The signal propagates coherently and nearly isotropically at electronic velocities (1.51×10^5 m/s) over distances of $\simeq 1 \mu\text{m}$. Theoretical calculations suggest that this anomalous propagation may arise due to a coupling between phonon modes and the phase mode of the EI (Fig. 1D). This provides a direct observation of collective modes of an EI system. Moreover, our model implies that the transition driving

the formation of the condensate is primarily excitonic in origin, and occurs in the BCS-BEC crossover region.

The sample consists of a flake of Ta_2NiSe_5 roughly 200 by 200 μm in size and 60 nm thick, exfoliated from a single crystal onto a glass slide. We characterize it by standard, non-spatially resolved pump-probe spectroscopy, as detailed in the Supplementary Materials Sec. I. Following this, we study the spatial dependence of the excitation in the material using femtosecond optical pump-probe microscopy, as illustrated in Fig 1B. In this technique, we perturb a small area of the sample using a diffraction limited ($\simeq 400$ nm full-width half-maximum) optical pulse of $\simeq 12$ fs duration. We measure the resulting change in transmission using a wide-field (15 μm full-width half-maximum), $\simeq 10$ fs probe pulse, which is projected onto an EMCCD camera. The large probe allows us to study both the directly excited area, and the surrounding material, imaging how excitations propagate in space and time as the presence of quasiparticles or oscillatory modes in the system modulate the probe transmission. Fig. 1B displays a schematic of the microscopy setup at the position of the sample and an example of a two-dimensional plot of the photoinduced transmissivity change ($\Delta T/T$) as measured 300 fs after the arrival of the pump pulse. ($\Delta T/T$) is obtained from $(T_{\text{pump on}} - T_{\text{pump off}})/(T_{\text{pump off}})$, where $T_{\text{pump on}}$ and $T_{\text{pump off}}$ indicate the transmission measured in the presence and in the absence of the pump pulse respectively.

The kinetics recorded at the photoexcited region as a function of the pump-probe delay time is shown in Fig. 1D (inset) and is analogous to those obtained in previous works using non-spatially resolved pump-probe spectroscopy [21, 27]. The signal is characterized by an exponentially decaying electronic component superimposed with a strong oscillating signal. In Fig. 1D we additionally report the Fourier Transform (FT) of this oscillatory component. The main recognizable features are the peaks at 1, 2.9 and 3.6 THz, which have been commonly associated with phonon modes in this system [21, 27].

The same FT analysis is now applied to the signal in areas away from the pump position, where no excitations are generated directly by the pump pulse. In this case, to focus on coherent propagation out of the photoexcited region and to maximize the signal-to-noise ratio, we average the $\Delta T/T$ signal over rings of pixels equidistant from the center (see Supplementary Materials Sec. II for details on the nearly isotropic nature of the signal). Through this procedure, we determine the spatial decay of the oscillatory modes by plotting the FT power density as a function of the ring distance, as shown in Fig. 2A for the 1, 2.9, and 3.6 THz modes. The resulting Gaussian shape is a convolution of the profile of the pump pulse (shown as a reference in Fig. 2B-D) and of the spatial propagation of the excited modes.

In Fig. 2B, we show the dependence of the FT power density spatial profile for the 2.9 THz mode on the pump

fluence. From a Gaussian fit of these curves we extract the half width at half maximum (HWHM), which is plotted in Fig. 2C. We do not observe a significant change in the HWHM up to $\simeq 0.55$ mJ/cm², after which the FT extension grows roughly linearly up to twice its original size, before finally saturating when we approach the material breaking point. This result suggests that at low fluences the signal is dominated by the profile of the pump pulse and only when the excitation surpasses a threshold the propagation of the mode outside the pumped region becomes visible. Interestingly, while an analogous behavior is observed for the 3.6 THz mode (see Supplementary Materials Sec. III), a rather different fluence dependence emerges for the 1 THz mode (Fig. 2C). This result hints at different microscopic mechanisms underlying the excitation of the oscillations.

We next compare (Fig. 2D) the spatial distribution of the FT power density of the 2.9 THz mode above and below T_c (see the Supplementary Materials Sec. III for analogous behavior in the 1 and 3.6 THz modes). While the data is normalized for ease of comparison, the fluence, the overall $\Delta T/T$ signal, and the absolute FT power density at the center of the pumped region are comparable for all these measurements. As T_c is approached from below, the FT profile narrows. Once the temperature surpasses T_c , the FT profile has shrunk to the size of the pump spot size, suggesting that above T_c the coherent propagation of the mode breaks down.

Returning to room temperature data, we further analyze the time traces for the different rings by performing continuous wavelet transforms (CWT) (see Supplementary Materials Sec. IV for more details). This procedure allows us to determine the amplitude of the oscillatory components as a function of time and distance from the photoexcited area. In Fig. 3A we show the results of this analysis for a few rings. It can be seen that the strongest amplitude for the 2.9 THz mode (the only one that is clearly traceable within the signal to noise limit) progressively shifts toward later times as we move farther away from the pump region. The position of this region in time is represented in Fig. 3B for all the rings. By performing a linear fit of this curve, focusing on ring radii residing outside of the directly pumped region, we extract a propagation velocity of $1.51 \pm 0.11 \times 10^5$ m/s. This means that below T_c the 2.9 THz mode coherently propagates, at a velocity characteristic of electronic excitations, for distances up to 1 μm .

We now discuss a potential origin of the anomalous spatial propagation at room temperature. First, we note that the measured propagation velocity is orders of magnitude larger than typical values both for optical phonons, which are commonly characterized by rather flat energy dispersions, and acoustic phonons, whose velocity is typically [35] below 10^3 m/s. This suggests that the propagating signal does not have a purely phononic origin. A possibility is the propagation of quasiparticles (QPs) emanating from the excitation spot with velocity $v_k = (\partial \epsilon_k / \partial k)$ of the order of 10^5 m/s, which can excite

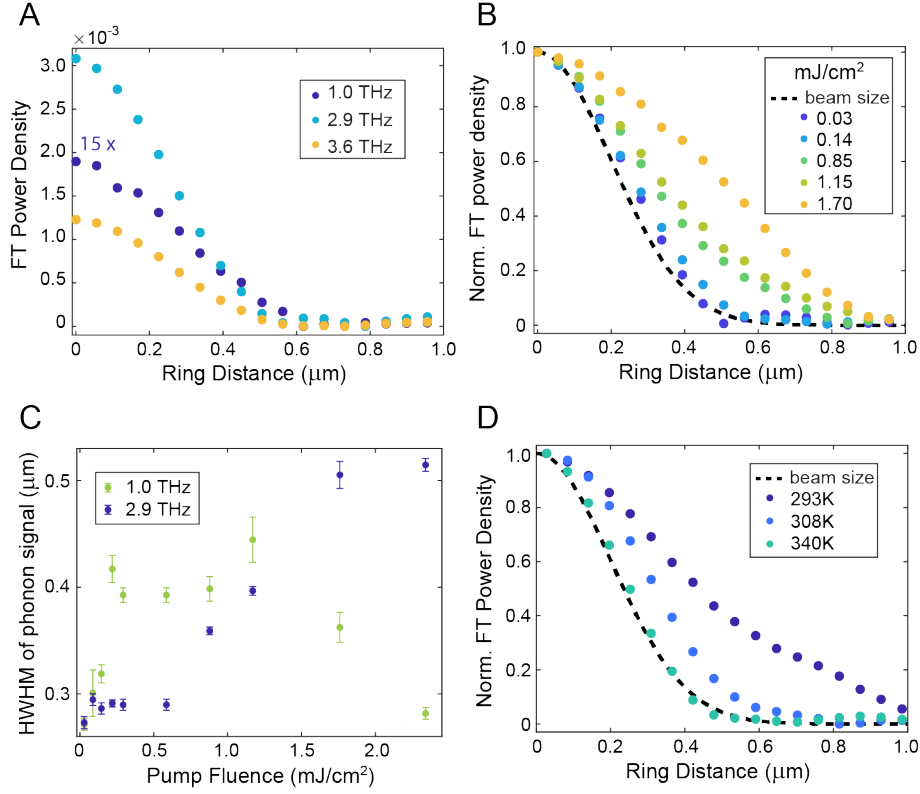


Figure 2. (A) Fourier Transform (FT) power density as a function of the distance of the ring over which we average the signal from the center of the pump region. This data was collected using a pump fluence of $0.3 \text{ mJ}/\text{cm}^2$. The data set for the 1 THz mode is magnified by a factor of 15 to improve its visibility. (B,D) Spatial dependence of the normalized FT power density for the 2.9 THz mode as a function of pump fluence (measured at room temperature) (B) and of temperature (each measured at a comparable fluence of $\simeq 1.2 \text{ mJ}/\text{cm}^2$) (D). The dashed line indicates the profile of the pump pulse. (C) Half-width half-maximum (HWHM) of the phonon spatial extension as a function of the pump fluence for the 1 THz and 2.9 THz modes.

phonons in their wake. However, at room temperature, the carrier relaxation time of QPs is usually only of the order of a few tens of femtoseconds, corresponding to a mean free path of a few nanometers [36, 37]. In addition, the emission of phonons by the QPs would generate oscillations that are not in phase as we move around the photoexcited region. In our experiments coherent behavior is observed on a much wider spatial range and on timescales extending to a few picoseconds. Another potential origin of the observed behavior is the excitation of rapidly propagating phonon-polaritons [38, 39]. However, in this case, we would expect to measure larger propagation velocities ($> 5 \times 10^6 \text{ m/s}$) due to the light-like nature of these modes (see Supplementary Materials Sec. VIII for more details) [40]. In addition, the disappearance of the propagation above T_c cannot be easily explained by this scenario, as the observed phonon modes characterize both the low and the high temperature phase of this material [27].

One remaining possibility for the anomalous propagation is the coupling between the phonon modes and the EI's collective phase mode. A phase mode is characterized by a linear dispersion and group velocities on the electronic scale. If an el-ph coupling is present, the phase

and the phonon modes can hybridize resulting in excitations of mixed electronic and phononic nature which can propagate at velocities close to that of the pure phase mode (see Fig. 1D). We expect that the lifetime of the phase mode can be significantly longer than that of QPs, as is supported by a theoretical calculation of the effects of the disorder on the QPs and the phase mode (see the Supplementary Materials Sec. IX and [41]). While the overall relaxation rate of the phonon-phase mode might not differ drastically from that of the phonons, the significantly higher speed can result in long propagation lengths ($\simeq \mu\text{m}$) for these excitations. The hybrid modes can then carry a phononic signature ballistically over long distances. This coupled phonon-phase mode scenario is also consistent with the suppression of propagation above T_c , where the collective phase mode should disappear. We note that a hybrid phonon-phase mode with an electronic-like group velocity is realized as long as the gap of the phase mode is comparable or smaller than the phonon energy. This occurs regardless of the origin of the gap, even where additional electronic terms directly breaking the symmetry [29, 30] also contribute to the formation of the gap.

Returning to Fig. 2C, we can tentatively interpret the

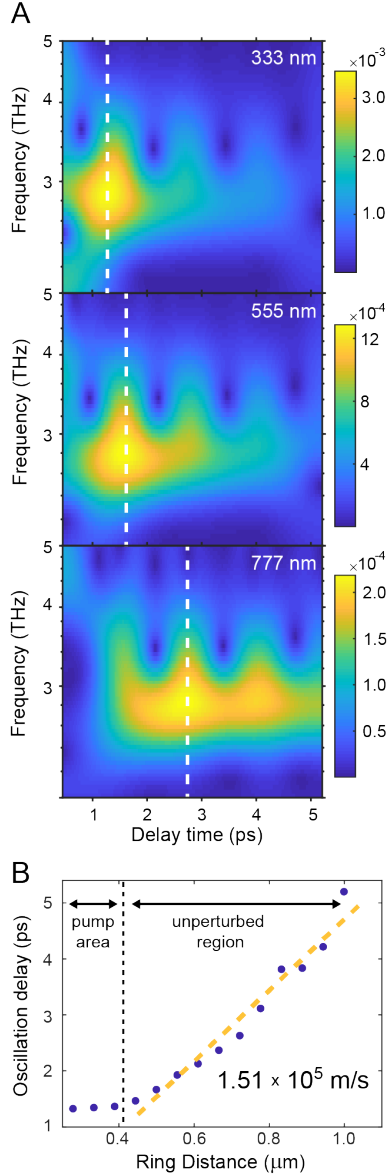


Figure 3. (A) Continuous wavelet transform (CWT) of the oscillatory component of the $\Delta T/T$ signal at three different distances (333, 555, and 777 nm) from the center of the pump region and measured at a fluence of $\simeq 1.6 \text{ mJ/cm}^2$. The color map represents the magnitude of the CWT. The white dotted lines approximately mark the location of the strongest phonon oscillations. The periodic oscillations in the CWT are clearly resolved and their possible origins are discussed in the main text. (B) Time delay of the region of strong oscillations as a function of the ring distance. The orange dashed line represents the linear fit of the data in the region outside the pump area and has an inverse slope $1.51 \times 10^5 \text{ m/s}$.

different behavior of the two oscillatory modes as the result of a different coupling process between these phonons and the phase mode (see Supplementary Materials Sec. VI). As the hybridization between the two modes occurs at larger wavevector with increasing phonon frequency, we expect that a higher order process, like Raman scat-

tering involving multiple phonon modes, could be required to excite the more energetic modes at wavevectors that are not provided by the focused laser beam (see Supplementary Materials Sec. V). Intriguingly, the saturation and drop in the 1 THz extension at high fluences could be the signature of the enhancement of the gap in the phase mode dispersion. If raised above the phonon energy, the phase mode would indeed not conduce to the formation of the hybrid modes. Further studies that go beyond the scope of this work are required to address these hypothesis.

To support our interpretations, we develop a theoretical model within a two band approximation. We start from a typical Hubbard-type Hamiltonian with additional terms for the el-ph coupling and the phonon energy,

$$H = H_{\text{kin}} + H_{\text{int}} + H_{\text{el-ph}} + H_{\text{ph}} \quad (1)$$

where H_{kin} represents the electronic bands, H_{int} is the electron-electron interaction, $H_{\text{el-ph}}$ is the el-ph coupling, and H_{ph} is the phonon Hamiltonian. This approach is analogous to that used in previous theoretical works on Ta_2NiSe_5 [19, 42, 43], and like there we use a form of $H_{\text{el-ph}}$ that explicitly breaks the symmetry of H (see Supplementary Materials Sec. VIIA and [44] for more details and for an analysis of the opposite case with no explicit symmetry breaking). The microscopical parameters corresponding to the band structure and the el-el interaction were estimated by fitting previous experimental ARPES results [19] (see Supplemental Materials Sec. VIIB). In Fig. 4A, the calculated linear response function shows the dispersion of the massless phase mode in a pure EI phase. Using this dispersion, the estimated group velocity is $v_{\text{phase}} = 1.0 \times 10^5 \text{ m/s}$ for this mode, which is of the same order of magnitude of the velocity observed in the experiments. In Fig 4b, we show the result in the presence of the el-ph coupling term where the phase mode becomes massive and a hybridization between the phase and phonon mode occurs.

In order to see whether the phonon oscillations induced by the excitation can propagate at velocities of the order of v_{phase} (an electronic-like velocity), we perform a real-space time-dependent mean-field simulation (see Supplementary Materials section VIIA). Here, we use a larger phonon frequency (indicated by the red, dashed line in Fig 4B, D-F), than those observed in the experimental data and we correspondingly consider a smaller excitation area. These assumptions do not affect the conclusions that we can draw from these calculations and they are adopted only for the sake of simplicity of the numerical simulation. In Fig 4C, we show the propagation of the phonon displacement after a spatially confined excitation. The signal propagates with a velocity of about $0.6 \times 10^5 \text{ m/s}$. We can visualize the time evolution of the phonon displacement at different distances from the excitation by performing a spatially windowed Fourier

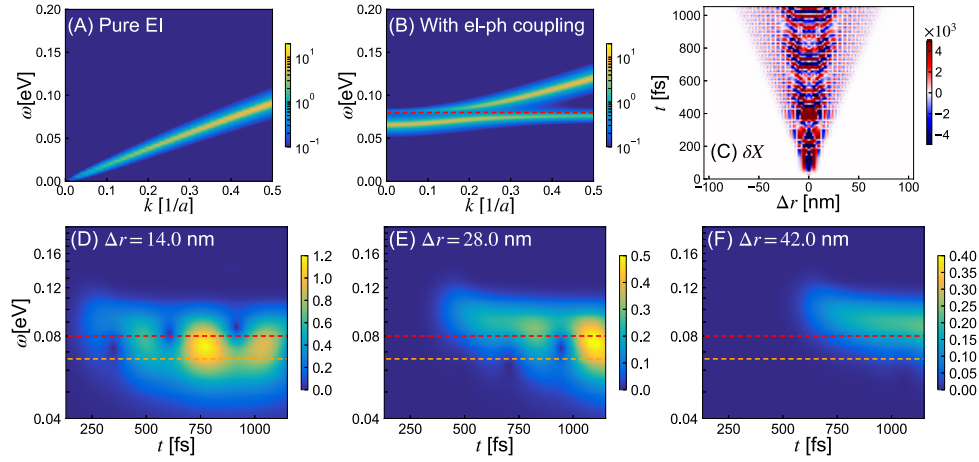


Figure 4. (A)(B) Response function of the order parameter for the microscopic two-band model on the one-dimensional lattice (A) with purely excitonic behavior and (B) in the presence of el-ph coupling which is small with respect to the Coulomb interaction and which explicitly breaks the continuous symmetry of the system. (C) Spatial and temporal evolution of the phonon displacement, δX for the case of non-zero el-ph coupling following an excitation at the center of the system at time $t = 0$, calculated within the mean-field description (D-F) Windowed Fourier transformation of the results in (C) at specified lattice sites, where Δr indicates the distance from the center of the excitation area. The red and orange dashed lines indicate the bare phonon frequency used in these calculations and the size of the phase mode gap respectively. The bandwidth of the conduction and valence bands is set to 1.6 eV and the Coulomb interaction to 0.84 eV. The corresponding band gap is about 0.32 eV.

transformation—analogue to a CWT analysis. The results are shown in Fig. 4D-F, where the orange dashed line indicates the frequency associated with the gap in the phase mode dispersion for the parameters used in our simulations. These plots illustrate the spreading of the hybrid mode at the phonon frequency with a velocity comparable to the phase mode velocity and further support the above scenario that mixing between the phase mode and the phonon mode leads to the fast propagation of the phonon oscillations.

We note that in Fig 4D-F, oscillations in the phonon displacement as a function of time contain information about the gap of the phase mode at $k \simeq 0$ (see the Supplementary Materials Sec. VII B1-2 for details). While the data in Fig. 3A shows analogous oscillations, we presently cannot determine if their origin is connected to the gapped phase mode or to a more trivial frequency beating between the 2.9 and 3.6 THz modes.

The picture that emerges from our measurements and theoretical considerations is one where a strong optical excitation promotes the ultrafast coherent generation of dispersionless (phonons) and dispersive collective (phase) modes of the excitonic condensate through the abrupt change in the quasi-particle density in the excitation region [45]. At energies where the optical phonon dispersion intersects the phase mode, coupled phonon-phason states can be excited and rapidly propagate outside the pumped region with velocity 1.5×10^5 m/s, remaining coherent up to $\simeq 1 \mu\text{m}$. Our results have several important implications. Firstly, they demonstrate that Ta_2NiSe_5 hosts an EI phase at room temperature, by providing a direct experimental observation of collective behavior in

a bulk EI candidate material and elucidating its interactions with the lattice degrees of freedom. Importantly, if the gap of the phase mode was much larger than the phonon frequency, the mixing between the modes would be suppressed. Hence, the effects of the el-ph coupling and of possible electronic terms that explicitly break the continuous symmetry [29–31, 42] should be weak, which indicates that the ordered phase in Ta_2NiSe_5 is mainly driven by interband Coulomb interactions (see Supplementary Materials Sec. VII). Another notable experimental observation is the small anisotropy in the mode propagation. This may seem counterintuitive since Ta_2NiSe_5 is a quasi-one-dimensional system and previous DFT calculations found that the bandwidth of the valence band along the direction perpendicular to the atomic chains should be almost five times smaller than in the direction along the chains [24]. However, we show theoretically that even in the presence of anisotropic hopping between the lattice sites, when the system approaches the BCS-BEC crossover regime, the anisotropy of the phase-mode velocity becomes small (see Supplementary Materials Sec. VIIB3). Hence, the small experimentally observed anisotropy indicates that the system is close to the BCS-BEC crossover regime, as suggested in previous works [25]. Although we argue that the velocity of the anomalously fast propagation is explained by the velocity of the collective phase mode, the precise non-linear process by which the collective mode is excited in Ta_2NiSe_5 remains to be clarified. Finally, we showcase the possibility of using spatially-resolved, femtosecond pump-probe measurements to gain crucial insights into the properties of solid-state systems manifesting emer-

gent many-body phenomena. By exciting and detecting coherent collective modes and by studying their propagation properties, important information can be gathered on the microscopic origin of these effects. Femtosecond pulses could thus provide a means to control and read out the properties of these systems in future quantum information applications.

ACKNOWLEDGMENTS

We thank the Engineering and Physical Sciences Research Council (EPSRC) and the Winton Programme for the Physics of Sustainability for funding. We also acknowledge funding from the European Research Council (ERC) under the European Union's Horizon 2020 re-

search and innovation programme (Grant Agreements 758826), EPSRC Grant No. EP/P034616/1 and by the Simons Foundation. The Flatiron Institute is a division of the Simons Foundation. Financial support was also received by Grant-in-Aid for Scientific Research from JSPS, KAKENHI Grant Nos. JP19K23425, JST CREST Grant No. JPMJCR1901, ERC Consolidator Grant No. 724103, and the Swiss National Science Foundation via NCCR Marvel. We thank the Department of Science and Technology, India for support under Nanomission and Year of Science Professorship. We thank Prof Surjit Singh for the help in preparation and characterization of the Ta_2NiSe_5 crystals. We acknowledge the support of the Cambridge International Trust and Wolfson College, Cambridge. The calculations were run on the Beo05 cluster at the University of Fribourg.

-
- * These authors contributed equally
- ¹ J. R. Schrieffer. *Theory of superconductivity*. CRC Press, 2018.
 - ² A. Behrle, T. Harrison, J. Kombe, K. Gao, M. Link, J.-S. Bernier, C. Kollath, and M. Köhl. Higgs mode in a strongly interacting fermionic superfluid. *Nature Physics*, 14(8):781–785, 2018.
 - ³ J. Kasprzak, M. Richard, S. Kundermann, A. Baas, P. Jeambrun, J. M. J. Keeling, F. M. Marchetti, M. H. Szymańska, R. André, J. L. Staehli, et al. Bose-Einstein condensation of exciton polaritons. *Nature*, 443(7110):409–414, 2006.
 - ⁴ D. Pekker and C. M. Varma. Amplitude/Higgs modes in condensed matter physics. *Annu. Rev. Condens. Matter Phys.*, 6(1):269–297, 2015.
 - ⁵ P. B. Littlewood and C. M. Varma. Amplitude collective modes in superconductors and their coupling to charge-density waves. *Physical Review B*, 26(9):4883, 1982.
 - ⁶ R. Shimano and N. Tsuji. Higgs mode in superconductors. *Annual Review of Condensed Matter Physics*, 11, 2019.
 - ⁷ P. W. Anderson. Plasmons, gauge invariance, and mass. *Physical Review*, 130(1):439, 1963.
 - ⁸ W. Zwerger. Anomalous fluctuations in phases with a broken continuous symmetry. *Physical review letters*, 92(2):027203, 2004.
 - ⁹ D. Jérôme, T. M. Rice, and W. Kohn. Excitonic insulator. *Physical Review*, 158(2):462, 1967.
 - ¹⁰ B. I. Halperin and T. M. Rice. Possible anomalies at a semimetal-semiconductor transition. *Reviews of Modern Physics*, 40(4):755, 1968.
 - ¹¹ L. V. Keldysh and A. N. Kozlov. Collective properties of excitons in semiconductors. *Sov. Phys. JETP*, 27(3):521, 1968.
 - ¹² P. Coleman. *Introduction to many-body physics*. Cambridge University Press, 2015.
 - ¹³ A. A. High, J. R. Leonard, A. T. Hammack, M. M. Fogler, L. V. Butov, A. V. Kavokin, K. L. Campman, and A. C. Gossard. Spontaneous coherence in a cold exciton gas. *Nature*, 483(7391):584, 2012.
 - ¹⁴ J. P. Eisenstein and A. H. MacDonald. Bose-Einstein condensation of excitons in bilayer electron systems. *Nature*, 432(7018):691–694, 2004.
 - ¹⁵ J. I. A. Li, T. Taniguchi, K. Watanabe, J. Hone, and C. R. Dean. Excitonic superfluid phase in double bilayer graphene. *Nature Physics*, 13(8):751, 2017.
 - ¹⁶ H. Cercellier, C. Monney, F. Clerc, C. Battaglia, L. Despont, M. G. Garnier, H. Beck, P. Aebi, L. Patthey, H. Berger, et al. Evidence for an excitonic insulator phase in 1T-TiSe₂. *Physical review letters*, 99(14):146403, 2007.
 - ¹⁷ C. Monney, C. Battaglia, H. Cercellier, P. Aebi, and H. Beck. Exciton condensation driving the periodic lattice distortion of 1T-TiSe₂. *Physical review letters*, 106(10):106404, 2011.
 - ¹⁸ Y. Hou, R. Wang, R. Xiao, L. McClintock, H. C. Travaglini, J. P. Francia, H. Fetsch, O. Erten, S. Y. Savrasov, B. Wang, et al. Millimetre-long transport of photogenerated carriers in topological insulators. *Nature communications*, 10(1):1–7, 2019.
 - ¹⁹ K. Seki, Y. Wakisaka, T. Kaneko, T. Toriyama, T. Konishi, T. Sudayama, N. L. Saini, M. Arita, H. Namatame, M. Taniguchi, et al. Excitonic Bose-Einstein condensation in Ta₂NiSe₅ above room temperature. *Physical Review B*, 90(15):155116, 2014.
 - ²⁰ S. Mor, M. Herzog, D. Golež, P. Werner, M. Eckstein, N. Katayama, M. Nohara, H. Takagi, T. Mizokawa, C. Monney, et al. Ultrafast electronic band gap control in an excitonic insulator. *Physical review letters*, 119(8):086401, 2017.
 - ²¹ D. Werdehausen, T. Takayama, M. Höppner, G. Albrecht, A. W. Rost, Y. Lu, D. Manske, H. Takagi, and S. Kaiser. Coherent order parameter oscillations in the ground state of the excitonic insulator Ta₂NiSe₅. *Science advances*, 4(3):eaap8652, 2018.
 - ²² A. Kogar, M. S. Rak, S. Vig, A. A. Husain, F. Flicker, Y. I. Joe, L. Venema, G. J. MacDougall, T. C. Chiang, E. Fradkin, et al. Signatures of exciton condensation in a transition metal dichalcogenide. *Science*, 358(6368):1314–1317, 2017.
 - ²³ Y. Wakisaka, T. Sudayama, K. Takubo, T. Mizokawa, M. Arita, H. Namatame, M. Taniguchi, N. Katayama, M. Nohara, and H. Takagi. Excitonic insulator state in Ta₂NiSe₅ probed by photoemission spectroscopy. *Physical review letters*, 103(2):026402, 2009.

- ²⁴ T. Kaneko, T. Toriyama, T. Konishi, and Y. Ohta. Orthorhombic-to-monoclinic phase transition of Ta_2NiSe_5 induced by the Bose-Einstein condensation of excitons. *Physical Review B*, 87(3):035121, 2013.
- ²⁵ Y. F. Lu, H. Kono, T. I. Larkin, A. W. Rost, T. Takayama, A. V. Boris, B. Keimer, and H. Takagi. Zero-gap semiconductor to excitonic insulator transition in Ta_2NiSe_5 . *Nature communications*, 8:14408, 2017.
- ²⁶ K. Okazaki, Y. Ogawa, T. Suzuki, T. Yamamoto, T. Someya, S. Michimae, M. Watanabe, Y. Lu, M. Nohara, H. Takagi, et al. Photo-induced semimetallic states realised in electron-hole coupled insulators. *Nature communications*, 9(1):1–6, 2018.
- ²⁷ S. Mor, M. Herzog, J. Noack, N. Katayama, M. Nohara, H. Takagi, A. Trunschke, T. Mizokawa, C. Monney, and J. Stähler. Inhibition of the photoinduced structural phase transition in the excitonic insulator Ta_2NiSe_5 . *Physical Review B*, 97(11):115154, 2018.
- ²⁸ T. Kaneko, B. Zenker, H. Fehske, and Y. Ohta. Competition between excitonic charge and spin density waves: Influence of electron-phonon and Hund’s rule couplings. *Physical Review B*, 92(11):115106, 2015.
- ²⁹ G. Mazza, M. Rösner, L. Windgätter, S. Latini, H. Hübener, A. J. Millis, A. Rubio, and A. Geroges. Nature of symmetry breaking at the excitonic insulator transition: Ta_2NiSe_5 . *arXiv preprint arXiv:1911.11835*, 2019.
- ³⁰ M. D. Watson, I. Marković, E. A. Morales, P. Le Fèvre, M. Merz, A. A. Haghighirad, and P. D. C. King. Band hybridisation at the semimetal-semiconductor transition of Ta_2NiSe_5 enabled by mirror-symmetry breaking. *arXiv preprint arXiv:1912.01591*, 2019.
- ³¹ B. Zenker, H. Fehske, and H. Beck. Fate of the excitonic insulator in the presence of phonons. *Physical Review B*, 90(19):195118, 2014.
- ³² G. V. Hartland. Ultrafast studies of single semiconductor and metal nanostructures through transient absorption microscopy. *Chemical Science*, 1(3):303–309, 2010.
- ³³ C. Schnedermann, J. Sung, R. Pandya, S. D. Verma, R. Y. S. Chen, N. Gauriot, H. M. Bretscher, P. Kukura, and A. Rao. Ultrafast tracking of exciton and charge carrier transport in optoelectronic materials on the nanometer scale. *The journal of physical chemistry letters*, 10(21):6727–6733, 2019.
- ³⁴ J. Sung, C. Schnedermann, L. Ni, A. Sadhanala, R. Y. S. Chen, C. Cho, L. Priest, J. M. Lim, H.-K. Kim, B. Monserrat, et al. Long-range ballistic propagation of carriers in methylammonium lead iodide perovskite thin films. *Nature Physics*, 16(2):171–176, 2020.
- ³⁵ V. S. Gorelik and N. S. Vasil’ev. Dispersion of optical and acoustic phonons in diamond and germanium crystals. *Inorganic Materials*, 48(5):462–468, 2012.
- ³⁶ D. Gall. Electron mean free path in elemental metals. *Journal of Applied Physics*, 119(8):085101, 2016.
- ³⁷ A. Jablonski, P. Mrozek, G. Gergely, M. Menhyard, and A. Sulyok. The inelastic mean free path of electrons in some semiconductor compounds and metals. *Surface and interface analysis*, 6(6):291–294, 1984.
- ³⁸ S. Dai, Z. Fei, Q. Ma, A. S. Rodin, M. Wagner, A. S. McLeod, M. K. Liu, W. Gannett, W. Regan, K. Watanabe, et al. Tunable phonon polaritons in atomically thin van der waals crystals of boron nitride. *Science*, 343(6175):1125–1129, 2014.
- ³⁹ D. N. Basov, M. M. Fogler, and F. J. G. De Abajo. Polaritons in van der waals materials. *Science*, 354(6309):aag1992, 2016.
- ⁴⁰ M. Mrejen, L. Yadgarov, A. Levanon, and H. Suchowski. Transient exciton-polariton dynamics in WSe_2 by ultrafast near-field imaging. *Science advances*, 5(2):eaat9618, 2019.
- ⁴¹ B. Remez and N. R. Cooper. Effects of disorder on the transport of collective modes in an excitonic condensate. *arXiv preprint arXiv:2003.10836*, 2020.
- ⁴² Y. Murakami, D. Golež, M. Eckstein, and P. Werner. Photoinduced enhancement of excitonic order. *Phys. Rev. Lett.*, 119:247601, 2017.
- ⁴³ K. Sugimoto, S. Nishimoto, T. Kaneko, and Y. Ohta. Strong coupling nature of the excitonic insulator state in Ta_2NiSe_5 . *Physical review letters*, 120(24):247602, 2018.
- ⁴⁴ Y. Murakami, D. Golež, M. Kaneko, A. Koga, A. Millis, and P. Werner. Collective modes in excitonic insulators: Effects of electron-phonon coupling and signatures in the optical response. *arXiv preprint arXiv:2003.10799*, 2020.
- ⁴⁵ T. K. Cheng, J. Vidal, H. J. Zeiger, G. D. M. S. Dresselhaus, M. S. Dresselhaus, and E. P. Ippen. Mechanism for displacive excitation of coherent phonons in Sb, Bi, Te, and Ti_2O_3 . *Applied Physics Letters*, 59(16):1923–1925, 1991.
- ⁴⁶ H. L. Stern, Cheminal A., Yost S. R., K. Broch, S. L. Bayliss, K. Chen, M. Tabachnyk, K. Thorley, N. Greenham, Hodgkiss, et al. Vibronically coherent ultrafast triplet-pair formation and subsequent thermally activated dissociation control efficient endothermic singlet fission. *Nat. Chem.*, 9:1205, 2017.
- ⁴⁷ A. Dubietis, G. Tamošauskas, R. Šuminas, V. Jukna, and A. Couairon. Ultrafast supercontinuum generation in bulk condensed media. *arXiv preprint arXiv:1706.04356*, 2017.
- ⁴⁸ K. Seki, Y. Wakisaka, T. Kaneko, T. Toriyama, T. Konishi, T. Sudayama, N. L. Saini, M. Arita, H. Namatame, M. Taniguchi, et al. Excitonic bose-einstein condensation in Ta_2NiSe_5 above room temperature. *Phys. Rev. B*, 90:155116, 2014.
- ⁴⁹ K. Sugimoto, S. Nishimoto, T. Kaneko, and Y. Ohta. Strong coupling nature of the excitonic insulator state in Ta_2NiSe_5 . *Phys. Rev. Lett.*, 120:247602, 2018.
- ⁵⁰ T. Kaneko, T. Toriyama, T. Konishi, and Y. Ohta. Orthorhombic-to-monoclinic phase transition of Ta_2NiSe_5 induced by the bose-einstein condensation of excitons. *Phys. Rev. B*, 87:035121, 2013.
- ⁵¹ G. D. Mahan. *Many-particle physics*. Springer Science & Business Media, 2013.
- ⁵² T. I. Larkin, R. D. Dawson, M. Höppner, T. Takayama, M. Isobe, Y.-L. Mathis, H. Takagi, B. Keimer, and A. V. Boris. Infrared phonon spectra of quasi-one-dimensional Ta_2NiSe_5 and Ta_2NiS_5 . *Phys. Rev. B*, 98:125113, 2018.
- ⁵³ A. L. Fetter and J. D. Welecka. *Quantum Theory of Many-Particle Systems*. Dover, New York, 2003.

Supplementary Material for:

Imaging the coherent propagation of collective modes in the excitonic insulator candidate Ta_2NiSe_5 at room temperature

Paolo Andrich,^{1,*} Hope M. Bretscher,^{1,*} Yuta Murakami,² Denis Golež,²
Benjamin Remez,¹ Prachi Telang,³ Anupam Singh,³ Luminita Harnagea,³ Nigel R.
Cooper,¹ Andrew J. Millis,^{2,4} Philipp Werner,⁵ A. K. Sood,⁶ and Akshay Rao¹

¹*Cavendish Laboratory, University of Cambridge, Cambridge CB3 0HE, United Kingdom*

²*Center for Computational Quantum Physics, Flatiron Institute, New York, New York 10010, USA*

³*Department of Physics, Indian Institute of Science Education and Research, Pune, Maharashtra 411008, India*

⁴*Department of Physics, Columbia University, New York, New York 10027, USA*

⁵*Department of Physics, University of Fribourg, Fribourg 1700, Switzerland*

⁶*Department of Physics, Indian Institute of Science, Bangalore, Karnataka 560012, India*

(Dated: August 29, 2021)

In these supplementary notes, we report additional details of the experimental methods and data analysis introduced in the main text. In addition, we present the theoretical models used to develop our interpretation. In Sec. I, we show the results of the material characterization performed using broadband, non-spatially resolved, transient reflection measurements. In Sec. II we comment on the spatial isotropy of the detected signal. In Sec. III we present the behavior as a function of fluence and temperature of the phonon modes that are not directly presented in the main text. In Sec. IV we report the details of the wavelet analysis used to extract information on the hybrid phase-phonon mode propagation. In Sec. V we propose a simple calculation to determine the range of wavevectors that are accessible in our measurements through first order excitation processes. In Sec. VI, we introduce a classical model of two coupled modes to provide a simple picture of coupling between the phase mode and the phonon mode. In Sec. VII, we introduce a microscopic two-band model coupled to phonons to study the properties of the collective modes of the excitonic insulating (EI) phase. Then, we provide the results of the linear response functions of the order parameters and the real-space simulation based on the mean-field theory. In Sec. VIII, we discuss the phonon-polariton in Ta_2NiSe_5 (TNS) and estimate its characteristic length scale and velocity. In Sec. IX, we discuss the disorder effects to the quasi-particles and the collective phase mode in the EI phase.

I. CHARACTERIZATION OF Ta_2NiSe_5 RESPONSE WITH FEMTOSECOND PUMP-PROBE SPECTROSCOPY

We characterize the material's temporal response using standard (non-spatially resolved), transient reflection measurements, in the configuration depicted in Fig. S1(a). Details of the setup are described in previous works from our group [46]. We perform the reflection measurements on a flake of Ta_2NiSe_5 roughly 200 by 200

μm in size and 300 nm thick exfoliated on a glass substrate and encapsulated using a second glass slide sealed with glue on all sides. Linearly polarized pump and probe pulses are focused onto the sample with spot sizes of 340 and 90 μm respectively, with the pump being larger to ensure uniform excitation of the probed region. The reflected probe pulse is collected and sent to a CCD camera for detection.

As Ta_2NiSe_5 absorbs electromagnetic radiation over the whole visible spectrum, we select the central wavelength of the pump pulse (690 nm) only for its ease of generation (through noncollinear optical parametric amplification) and compression. Using autocorrelation measurements we determine the temporal length of the pump pulse to be < 10 fs. The pump polarization with respect to the crystal axis is found to have no significant effect on the signal, contrary to previous reports [21]. The broadband probe pulse (500-950 nm) is obtained as the result of a supercontinuum generation process in a YAG crystal using 100 fs, 1042 nm high energy pulses [47].

The evolution of the reflected signal as a function of the probe wavelength is represented in Fig. S1(b) for a few pump-probe time delays. In Fig. S1(c) we show the kinetics for the signal integrated over the highlighted region of Fig. S1(b), which is the wavelength range considered in the spatially resolved measurements. Note that the sign of the transient signal, which is negative when measured in transmission, was reversed in the plots presented in the main text to simplify the discussion and analysis of the data. As this sign only carries information on the specific transient changes of the dielectric function of the material at optical wavelengths, it has no implications for our current discussion.

II. INVESTIGATION OF THE SPATIAL ISOTROPY OF THE SIGNAL

We investigate how the choice of the integration path used to analyze the two-dimensional $\Delta T/T$ data affects the interpretation of the oscillatory modes spatial extent.

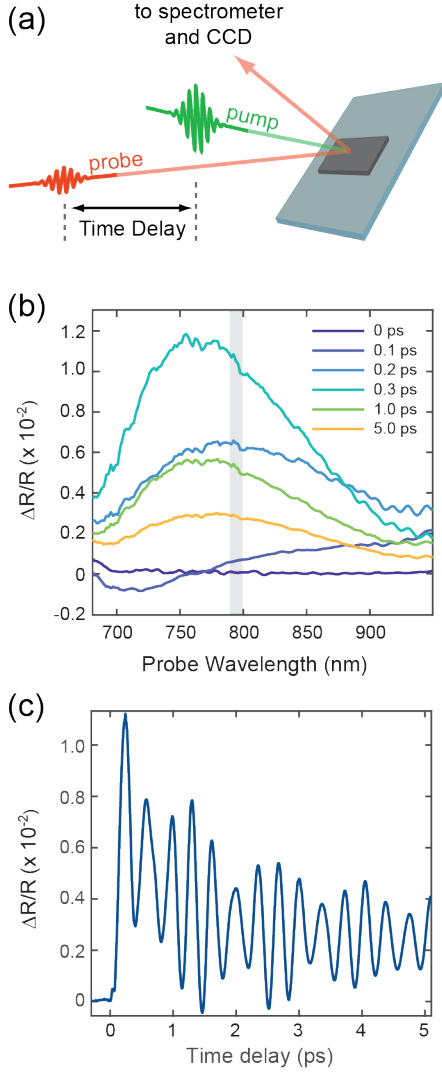


Figure S1. Characterization of the femtosecond dynamic of the system. (a) Schematic of the pump-probe, transient reflection setup. (b) Transient reflection spectra in the 680 - 950 nm range for a few probe time delays. The data was corrected to compensate for the temporal chirp of the broadband probe pulse. The direct comparison of the $\Delta R/R$ values between the different spectra is complicated by the existence of the strong phononic oscillations. (c) Time dependence of the $\Delta R/R$ signal averaged between 790 and 800 nm. No significant differences in the kinetics are observed at different wavelengths.

In particular we repeat the calculation used to obtain the curves in Fig. 2A using an elliptical path with axis ratio 1.2 and 2. As shown in Fig. S2 for the case of the 2.9 THz mode, the resulting oscillation extension is always smaller when calculated over an elliptical path, suggesting that the signal is highly isotropic in nature and is coherent along the circular paths. However, small changes are detectable as we rotate the orientation of the ellipses axes, which might be a sign of a residual small anisotropy. Nonetheless, this effect cannot be easily disentangled from a possible presence of slight anisotropies

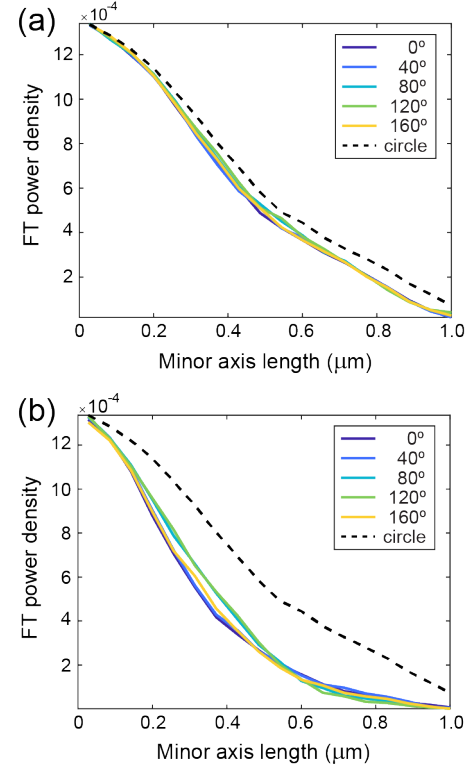


Figure S2. Fourier Transform power density calculated from data averaged over elliptical paths of axis ratio (a) 1:1.2 and (b) 1:2. The angle refers to the orientation of the major axis of the ellipses with respect to the horizontal axis of the CCD camera image.

in the pump spot and requires further investigation.

III. BEHAVIOR OF OTHER PHONON MODES

Here we report additional data on the behavior of the phonon oscillations that were not explicitly addressed in the main text. Figure S3 shows the evolution of the half width at half maximum (HWHM) for the 3.6 THz mode as a function of the pump fluence. Comparing this result with the one presented in Fig. 2C of the main text we can see that this mode behaves very similarly to the 2.9 THz one.

In Fig. S4 we present the spatial distribution of the Fourier Transform (FT) power density for the 1 and 3.6 THz modes above and below T_c . These show a trend similar to what is reported for the 2.9 THz mode in the main text.

IV. DETAILS OF THE WAVELET ANALYSIS

The continuous wavelet transform (CWT) is performed using the MATLAB® wavelet toolbox. We used in particular the Generalized Morse Wavelet with 48 voices per octave for all the data reported here and in the main text.

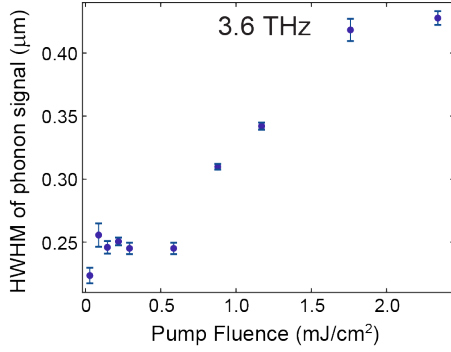


Figure S3. Evolution of the half width at half maximum (HWHM) of the 3.6 THz mode spatial distribution as a function of the pump fluence. The HWHM values are obtained through a gaussian fit of the magnitude of the 3.6 THz FT peak as a function of the distance of the signal from the center of the pump spot.

We also performed the analysis using the Bump Wavelet with similar results but the Generalized Morse Wavelet guarantees the best temporal resolution.

In Fig. S5(a) we show the results of this analysis for a complete series of 18 rings at progressively increasing distances from the pump center. As also seen in Fig. 3A in the main text, the magnitude of the phonon modes shows periodic oscillations in time. We currently cannot determine whether this beating is related to the gap in the phase mode dispersion (see VII A) or beating between the 2.9 and 3.6 THz modes. The beating introduces an uncertainty in the identification of the position of the maximum of the 2.9 THz oscillations in time.

The data for the rings further away from the center clearly show the presence of a sizeable signal at early pump-probe time delays. This signal is associated to the diffraction of the probe pulse through the photoexcited region, in a common Airy disks pattern. This is a consequence of the change in the refractive index induced by the tightly focused pump (established within a few tens of femtoseconds). As the broader (plane-wave-like) probe pulse transmits through the material, it experiences different phase retardation as it passes through the region of the pump with respect to the outside area. This results in the generation of a diffraction pattern typical of a plane wave going through a pinhole.

In Fig. S5(c) we report the value of the oscillation maximum as a function of the ring distance both for the “traveling” wave and for the signal at early times (measured at 0.5 ps). It can be clearly seen that, while the signal associated with the propagating mode decays monotonically throughout the whole range, the early time signal follows a typical diffraction pattern. This result shows that with this analysis we can separate the contribution of the propagating modes excited in the system and study their dynamics.

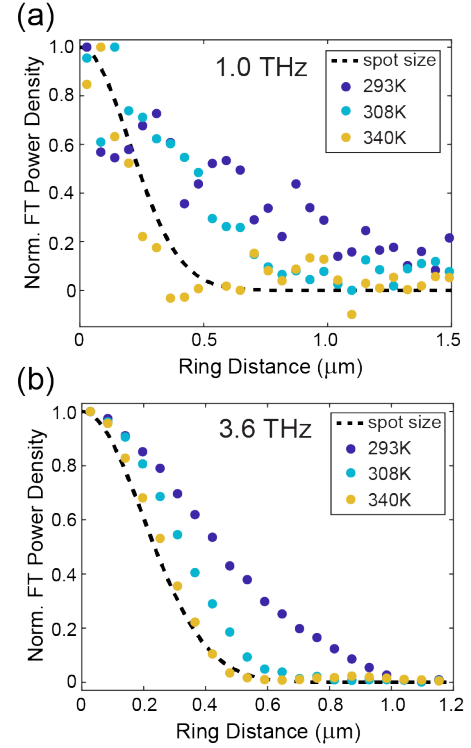


Figure S4. Normalized Fourier Transform (FT) power density as a function of the ring distance measured at three different temperatures for (a) the 1 THz and (b) the 3.6 THz modes. As in the main text the comparison was obtained between measurements with similar $\Delta T/T$ amplitudes and using analogous fluences. The dashed line indicates schematically the extension of the pumped region.

V. NOTES ON ACCESSIBLE WAVEVECTOR TRANSFERS

We can estimate the range of in-plane wavevector transfers accessible in our measurements by simply considering the numerical aperture (NA) of the objective that focuses the pump pulse. Figure S6 schematically illustrates the experimental conditions of our setup. The objective has a 1.1 NA, which translates into a half collection angle of $\sim 46^\circ$. Starting from the wavevector k of a monochromatic light at 690 nm we can then obtain $\sim 6.6 \times 10^4 \text{ cm}^{-1}$ as the maximum available in-plane component k_\perp .

We can now compare this result with the wavevector k of the hybrid phonon-phase modes estimated using its group velocity v and assuming a roughly linear dispersion for the mode frequency ω ($k \sim \omega/v$). Using the velocity extracted in the main text ($v = 1.51 \times 10^5 \text{ m/s}$) we would obtain $k \sim 4 \times 10^5 \text{ cm}^{-1}$ for a hybrid mode of the phase mode and the 1 THz phonon. As we are neglecting the effect of the hybridization between the phonon and the phase mode (with the relative anticrossing behavior as sketched in Fig. 1D), this estimate is an upper bound for the real wavevector. From this we can suggest that, while the wavevector for a 1 THz mode might be directly

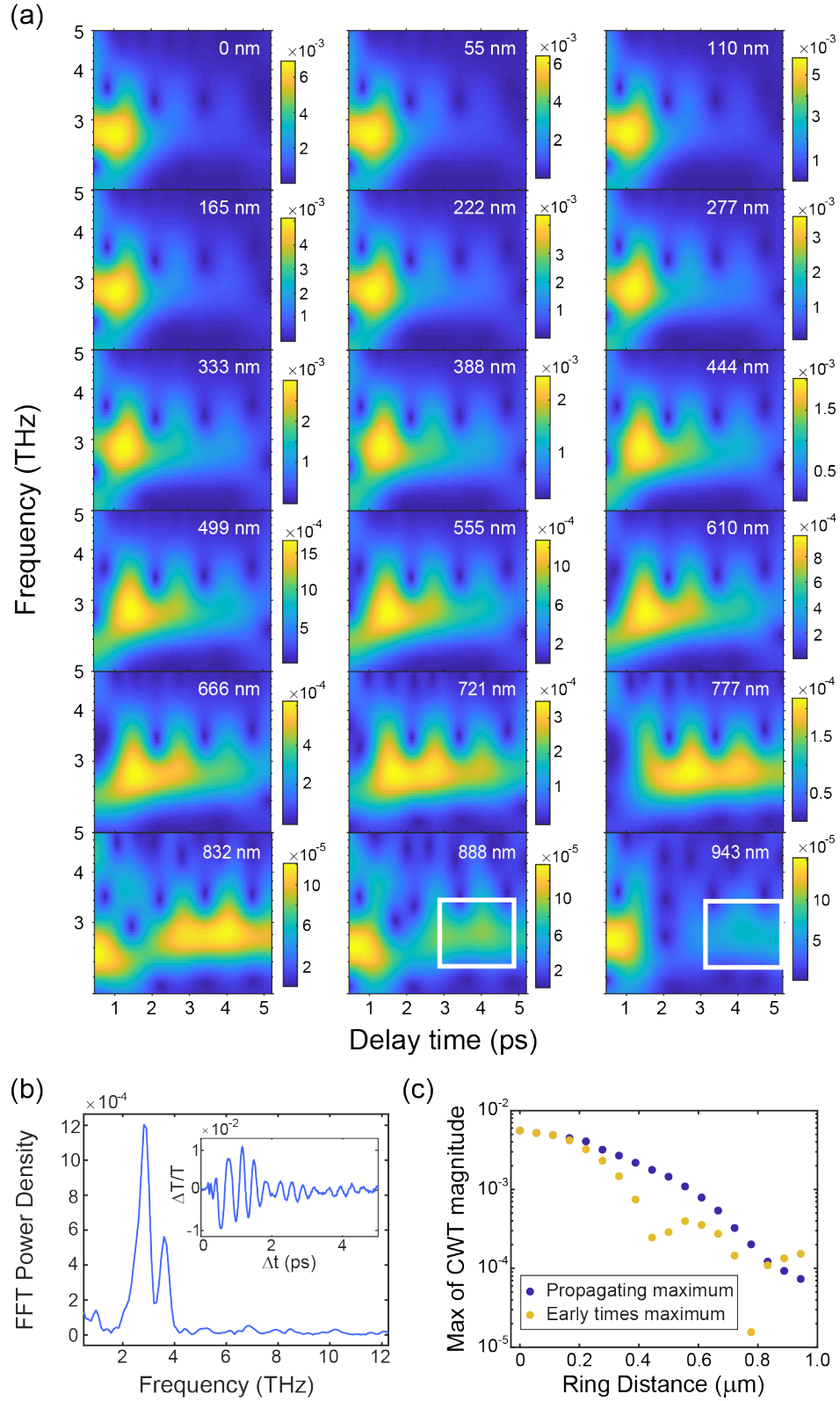


Figure S5. Details of the CWT analysis. (a) Plots of the continuous wavelet transform (CWT) of the signal for a series of rings at progressively larger distances from the center of the pump region. The color map indicates the magnitude of the CWT. (b) Kinetics of the oscillatory component of the signal collected in the center of the pump region. Visible in the data is the presence of collapses and revivals of some of the oscillations associated with the beating between different modes. (c) Maximum of the wavelet transform magnitude obtained for the propagating signal (blue circles) and for the signal at early delay times (yellow circles).

accessible through a linear process, it is possible that this is not the case for a 2.9 THz mode, which would require a higher order mechanism. This consideration might explain the different behavior as a function of the pump fluence observed in Fig. 2C. A more detailed description of the hybrid modes excitation process, which is beyond the scope of this work, is necessary to further investigate this hypothesis.

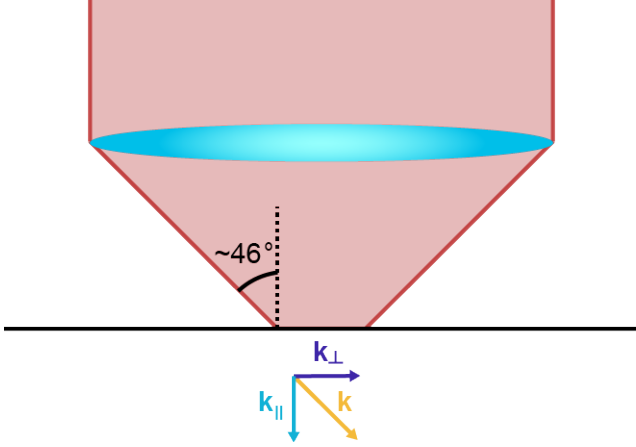


Figure S6. Schematic representation of the focusing effect of an objective and its consequence on the magnitude of the light wavevector components.

VI. CLASSICAL MODEL OF TWO COUPLED MODES

In the main text, we proposed a potential origin of the fast propagation of the phonon oscillation, namely the coupling between the collective phase mode in the ordered phase and the phonon mode. Although this scenario can be directly analyzed with a microscopic model as in the following section, let us start with the minimal model that describes this picture to gain some intuition. The minimal model describes coupled classical modes; one represent the dispersive phase mode (ϕ) and the other is the non-dispersive phonon mode (X). In the absence of damping, the equations of motions are

$$\partial_t^2 X_{\mathbf{k}}(t) + \omega_0^2 X_{\mathbf{k}}(t) - \alpha^2 \phi_{\mathbf{k}}(t) = f_X(\mathbf{k}, t), \quad (2)$$

$$\partial_t^2 \phi_{\mathbf{k}}(t) + (\Delta^2 + v^2 \mathbf{k}^2) \phi_{\mathbf{k}}(t) - \alpha^2 X_{\mathbf{k}}(t) = f_\phi(\mathbf{k}, t), \quad (3)$$

where the f s describe the forces from the applied excitation, ω_0 is the phonon frequency, Δ is the gap of the phase mode, v is the velocity of the phase mode, α is the coupling between these two modes, and \mathbf{k} is the momentum. This equation has a Green function

$$\mathbf{D}_{\mathbf{k}}(t) = \mathbf{R}_{\mathbf{k}} \begin{pmatrix} \frac{\sin[\Omega_+(\mathbf{k})t]}{\Omega_+(\mathbf{k})} & 0 \\ 0 & \frac{\sin[\Omega_-(\mathbf{k})t]}{\Omega_-(\mathbf{k})} \end{pmatrix} \mathbf{R}_{\mathbf{k}}^{-1} \quad (4)$$

where $\mathbf{R}_{\mathbf{k}}$ is the rotation that diagonalizes the force matrix at \mathbf{k} and

$$\Omega_{\pm}^2(\mathbf{k}) = \frac{1}{2} \left(\omega_0^2 + \Delta^2 + v^2 k^2 \pm \sqrt{(\omega_0^2 - \Delta^2 - v^2 k^2)^2 + 4\alpha^4} \right). \quad (5)$$

In general, we have

$$\begin{pmatrix} X(\mathbf{r}, t) \\ \phi(\mathbf{r}, t) \end{pmatrix} = \quad (6)$$

$$\int^t dt' \int \frac{d\mathbf{k}}{(2\pi)^d} e^{i\mathbf{k} \cdot \mathbf{r}} \mathbf{D}(\mathbf{k}, t - t') \begin{pmatrix} f_X(\mathbf{k}, t') \\ f_\phi(\mathbf{k}, t') \end{pmatrix}, \quad (7)$$

where d is the dimension. From this expression, one can naively see that mixing results in the propagation of the phonon mode at the scale of v .

To obtain further insights, we consider the case where $f_\phi(k, t) = \exp[-\frac{k^2}{k_c^2}] \delta(t)$ and $f_X = 0$. Then we simplify Eq. (7) by i) assuming $v^2 k_c^2, \Delta^2 \ll \omega_0^2$, ii) focussing on the propagating mode (neglecting the contribution from the upper (non-propagating) mode) and iii) working to leading order in α^2 . For the two dimensional system, for example, we obtain

$$\begin{pmatrix} X(r, t) \\ \phi(r, t) \end{pmatrix} = B_\phi(r, t) \begin{pmatrix} \frac{2\alpha^2}{\omega_0^2} \\ 1 \end{pmatrix} \quad (8)$$

with

$$B_\phi(r, t) = \int_0^\infty \frac{k dk}{2\pi} J_0(kr) \frac{\sin[\sqrt{\Delta^2 + v^2 k^2} t]}{\sqrt{\Delta^2 + v^2 k^2}} f_\phi(k), \quad (9)$$

where J_0 is the 0 th order Bessel function. Here, we note that we can obtain a similar form for the one-dimensional case.

When $\Delta = 0$, the expression becomes

$$B_\phi(r, t) = \frac{1}{vr} \int_0^\infty \frac{du}{2\pi} J_0(u) \sin[ur] e^{-\frac{u^2}{x^2}}, \quad (10)$$

where $k = u/r$, $t = \tau r/v$ and $r = x/k_c$. At distances longer than the pump size the $e^{-\frac{u^2}{x^2}}$ factor becomes unimportant and we just get $B = b(vt/r)/r$: a front propagating out. When $\Delta \neq 0$, we set $\tau = \Delta t$, $q = k\xi$, $r = x\xi$ with $\xi = v/\Delta$. Then, we obtain

$$B_\phi(r, t) = \frac{1}{\xi^2 \Delta} \int_0^\infty \frac{q dq}{2\pi} J_0(qx) \frac{\sin[\sqrt{1 + q^2} \tau]}{\sqrt{1 + q^2}} f_\phi(q/\xi). \quad (11)$$

Now we see that there is a natural scale for oscillations in time (Δ). Namely, this indicates that one can in principle identify the gap in the signal propagation, which is indeed confirmed by the microscopic simulation [see Fig. S10 in the next section].

VII. TIME EVOLUTION OF MICROSCOPIC MODEL

A. Formulation

1. Models

For the theoretical analysis of the collective modes in the EI phase, we consider a simple two-band spinless-fermion model coupled to two different types of phonons,

$$\hat{H} = \hat{H}_{\text{kin}} + \hat{H}_{\text{int}} + \hat{H}_{\text{el-ph}} + \hat{H}_{\text{ph}} + \hat{H}_{\text{el-ph2}} + \hat{H}_{\text{ph2}}. \quad (12)$$

The first term includes the kinetic term and the band energies

$$\hat{H}_{\text{kin}} = - \sum_{\langle i,j \rangle, a=0,1} J_a(\mathbf{r}_{ij}) \hat{c}_{i,a}^\dagger \hat{c}_{j,a} + \sum_{i,a} D_a \hat{c}_{i,a}^\dagger \hat{c}_{i,a}. \quad (13)$$

Here $\langle i, j \rangle$ indicates a pair of nearest-neighbor sites, and $a = 0, 1$ refers to the conduction band and the valence band, respectively. \hat{c}^\dagger is the electron creation operator, $J_a(\mathbf{r}_{ij})$ is the hopping parameter, \mathbf{r}_{ij} is the spatial vector connecting site j to site i , and D_a is the energy of band a . We also define the band-level splitting, $D_{01} = D_0 - D_1$. The dispersion of the free electrons is given by $\epsilon_a(\mathbf{k}) \equiv -\sum_l J_a(\mathbf{r}_l) e^{-i\mathbf{k} \cdot \mathbf{r}_l}$. For simplicity, we consider the local interaction given by

$$\hat{H}_{\text{int}} = U \sum_i \hat{n}_{i0} \hat{n}_{i1}. \quad (14)$$

Without el-ph couplings, the system has $U(1)$ symmetries and the number of particles in the valence band and the conduction band is separately conserved. At low enough temperatures, the system can break the symmetry, such that only the total number is conserved, and realize an EI phase. In particular, when the bandgap is at the Γ point ($\mathbf{k} = \mathbf{0}$), the system keeps the translational invariance in the EI phase, and we can introduce the order parameter of the phase as $\phi = \langle \hat{c}_{i,0}^\dagger \hat{c}_{i,1} \rangle$. In the following, we focus on this case and consider bands with opposite hopping, $J_0 = -J_1$, and half filling ($D_0 + D_1 = -U$). Similar types of two-band models have previously been used to successfully describe relevant features in TNS [42, 48, 49].

In general, there exists two types of electron-phonon (el-ph) couplings. The first type breaks the continuous symmetry and the second one does not. In this study, we consider

$$\hat{H}_{\text{el-ph}} = g \sum_i (\hat{b}_i^\dagger + \hat{b}_i) (\hat{c}_{i,1}^\dagger \hat{c}_{i,0} + \hat{c}_{i,0}^\dagger \hat{c}_{i,1}), \quad (15a)$$

$$\hat{H}_{\text{ph}} = \omega_0 \sum_i \hat{b}_i^\dagger \hat{b}_i, \quad (15b)$$

as an example of the first type phonon (“type 1 phonon”

). Here, \hat{b}^\dagger is its creation operator. This phonon reduces the $U(1)$ symmetry of the Hamiltonian down to a Z_2 symmetry. It cooperates with the intraband Coulomb interaction to trigger the phase transition, and it favors a real value of the order parameter ϕ (see [42]). We also introduce the effective coupling strength as $\lambda \equiv \frac{2g^2}{\omega_0}$. As an example of the second type of phonons (“type 2 phonon”) we consider

$$\hat{H}_{\text{el-ph2}} = g_2 \sum_i (\hat{b}_{i,2}^\dagger + \hat{b}_{i,2}) (\hat{n}_{i,0} - \hat{n}_{i,1}), \quad (16a)$$

$$\hat{H}_{\text{ph2}} = \omega_2 \sum_i \hat{b}_{i,2}^\dagger \hat{b}_{i,2}. \quad (16b)$$

Here, \hat{b}_2^\dagger is the corresponding creation operator, and we introduce $\lambda_2 = \frac{2g_2^2}{\omega_2}$. This phonon does not affect the symmetry of the system.

In the following analysis, we use the single-particle density matrix $\hat{\rho}_{ia,jb} \equiv \hat{c}_{jb}^\dagger \hat{c}_{ia}$ and we use $\hat{\rho}$ when we regard the density matrix as a matrix with indices (i, a) and (j, b) . We also define local density matrices as $\hat{\rho}_{\nu j} \equiv \hat{\Psi}_j^\dagger \boldsymbol{\sigma}_\nu \hat{\Psi}_j$. Here, $\hat{\Psi}_j^\dagger = [\hat{c}_{j0}^\dagger, \hat{c}_{j1}^\dagger]$ and $\boldsymbol{\sigma}_\nu$ are the Pauli matrices (with $\nu = 0$ corresponding to the identity matrix). In addition, we introduce the displacement and momentum of the phonons as $\hat{X}_i = \hat{b}_i + \hat{b}_i^\dagger$, $\hat{P}_i = \frac{1}{i}(\hat{b}_i - \hat{b}_i^\dagger)$, $\hat{X}_{i,2} = \hat{b}_{i,2} + \hat{b}_{i,2}^\dagger$ and $\hat{P}_{i,2} = \frac{1}{i}(\hat{b}_{i,2} - \hat{b}_{i,2}^\dagger)$. In the following, we denote the time-dependent expectation value of these quantities by $\rho_{ia,jb}(t)$, $\boldsymbol{\rho}(t)$, $\rho_{\nu j}(t)$, $X_i(t)$, $P_i(t)$, $X_{i,2}(t)$, $P_{i,2}(t)$, respectively.

2. Time-dependent mean-field theory

Now, we explain the time-dependent mean-field theory (tdMF) for model (12). In the tdMF, we decouple the Coulomb interaction term and the el-ph coupling term to obtain the MF Hamiltonians

$$\hat{H}_{\text{el}}^{\text{MF}}[\boldsymbol{\rho}, X, X_2](t) = \hat{H}_{\text{kin}} + \hat{H}^{\text{HF}}(t) + \hat{H}_{\text{el-ph}}^{\text{MF,el}}(t) + \hat{H}_{\text{el-ph2}}^{\text{MF,el}}(t), \quad (17a)$$

$$\hat{H}_{\text{ph}}^{\text{MF}}[\boldsymbol{\rho}](t) = \omega_0 \sum_i \hat{b}_i^\dagger \hat{b}_i + \sum_{l,\nu} g_{\nu} \rho_{\nu,l}(t) \hat{X}_l, \quad (17b)$$

$$\hat{H}_{\text{ph2}}^{\text{MF}}[\boldsymbol{\rho}](t) = \omega_2 \sum_i \hat{b}_{i,2}^\dagger \hat{b}_{i,2} + \sum_{l,\nu} g_{\nu,2} \rho_{\nu,l}(t) \hat{X}_{l,2}. \quad (17c)$$

Here, we use $[\boldsymbol{\rho}, X, X_2]$ and $[\boldsymbol{\rho}]$ to explicitly show the dependence of the MF Hamiltonian on the expectation value of the density matrix and the phonon displace-

ments. The MF terms in $\hat{H}_{\text{el}}^{\text{MF}}$ are

$$\hat{H}^{\text{HF}}[\boldsymbol{\rho}](t) = \sum_{l,\nu} U_{\nu} \rho_{\nu l}(t) \hat{\rho}_{\nu l}, \quad (18a)$$

$$\hat{H}_{\text{el-ph}}^{\text{MF,el}}[X](t) = \sum_{l,\nu} g_{\nu} X_l(t) \hat{\rho}_{\nu l}, \quad (18b)$$

$$\hat{H}_{\text{el-ph2}}^{\text{MF,el}}[X_2](t) = \sum_{l,\nu} g_{2,\nu} X_{l,2}(t) \hat{\rho}_{\nu l}, \quad (18c)$$

with $[U_0, U_1, U_2, U_3] \equiv [\frac{U}{2}, -\frac{U}{2}, -\frac{U}{2}, -\frac{U}{2}]$, $g_{\nu} \equiv \delta_{1,\nu} g$ and $g_{\nu,2} \equiv \delta_{3,\nu} g_2$.

In equilibrium, the electron MF Hamiltonian at half-filling reduces to

$$\hat{H}_{\text{el}}^{\text{MF}} = \frac{1}{2} \sum_{\mathbf{k}} \hat{\Psi}_{\mathbf{k}}^{\dagger} \begin{bmatrix} B_{\mathbf{k}}^z & B_{\mathbf{k}}^x - iB_{\mathbf{k}}^y \\ B_{\mathbf{k}}^x + iB_{\mathbf{k}}^y & -B_{\mathbf{k}}^z \end{bmatrix} \hat{\Psi}_{\mathbf{k}}, \quad (19)$$

where we have introduced the Fourier transform of the operator $\hat{\Psi}_{\mathbf{k}}^{\dagger} = \frac{1}{\sqrt{N}} \sum_{\mathbf{r}_i} e^{i\mathbf{k} \cdot \mathbf{r}_i} \hat{\Psi}_i^{\dagger}$. The elements are defined as

$$B_{\mathbf{k}}^x = -2(U + 2\lambda)\text{Re}\phi, \quad (20a)$$

$$B_{\mathbf{k}}^y = -2U\text{Im}\phi, \quad (20b)$$

$$B_{\mathbf{k}}^z = (\epsilon_0(\mathbf{k}) - \epsilon_1(\mathbf{k})) - (U + 2\lambda_2) \Delta n, \quad (20c)$$

where we have introduced the difference in the occupation $\Delta n = n_0 - n_1$ and used the equilibrium condition for the phonon distortion

$$P_i = 0, \quad X_i = -\frac{4g}{\omega_0} \text{Re}\phi, \quad (21a)$$

$$P_{i,2} = 0, \quad X_{i,2} = -\frac{2g_2}{\omega_2} \Delta n. \quad (21b)$$

From Eq. (20a), one can see that U and λ cooperatively contribute to the formation of the ordered phase.

The single-particle spectrum within the MF theory is given by $E_{\pm}(\mathbf{k}) = \pm \frac{1}{2} B_{\mathbf{k}}$ with $B_{\mathbf{k}} = \sqrt{(B_{\mathbf{k}}^x)^2 + (B_{\mathbf{k}}^y)^2 + (B_{\mathbf{k}}^z)^2}$. Hence, the MF self-consistency relation becomes

$$\phi = \frac{1}{N} \sum_{\mathbf{k}} \frac{B_{\mathbf{k}}^x + iB_{\mathbf{k}}^y}{2B_{\mathbf{k}}} [f(E_+(\mathbf{k}), T) - f(E_-(\mathbf{k}), T)], \quad (22a)$$

$$\Delta n = \frac{1}{N} \sum_{\mathbf{k}} \frac{B_{\mathbf{k}}^z}{B_{\mathbf{k}}} [f(E_+(\mathbf{k}), T) - f(E_-(\mathbf{k}), T)]. \quad (22b)$$

We solve this to obtain the equilibrium value of the MF parameters ϕ and Δn .

We can specify the system by a parameter set $(D_{01}, U, \lambda, \lambda_2)$. For $(D_{01}, U, \lambda, \lambda_2) = (D_{01,\text{ref}}, U_{\text{ref}}, 0, 0)$, we can determine the single-particle spectrum and the order parameter ϕ from Eqs. (20) and (22). However, Eqs. (20) and (22) imply that when $\lambda (\neq 0)$ and $\lambda_2 (\neq 0)$ are given, one can always adjust D_{01} and U such that this system shows the same single-particle spectrum and order parameter as the system with $(D_{01,\text{ref}}, U_{\text{ref}}, 0, 0)$. In the following, we specify the system by a parameter

set $[D_{01,\text{ref}}, U_{\text{ref}}, \lambda, \lambda_2]$ instead of $(D_{01}, U, \lambda, \lambda_2)$, which means that U and D_{01} are adjusted such that the single-particle spectrum and the order parameter are the same as those for $(D_{01,\text{ref}}, U_{\text{ref}}, 0, 0)$.

Next, we consider the case where the system is initially in equilibrium and excited at $t > 0$ by an external perturbation of the system, $\hat{H}_{\text{ex}}(t)$. Within tdMF, the time evolution of the system is determined by $\hat{\mathcal{U}}^{\text{MF}}(t) \equiv \mathcal{T} \exp \left(-i \int_0^t \hat{H}_{\text{tot}}^{\text{MF}}(t) \right)$ with \mathcal{T} denoting the time-ordering operator. The time-dependent Hamiltonian is given by

$$\begin{aligned} \hat{H}_{\text{tot}}^{\text{MF}}[\boldsymbol{\rho}, X, X_2](t) = & \hat{H}_{\text{el}}^{\text{MF}}[\boldsymbol{\rho}, X, X_2](t) + H_{\text{ph}}^{\text{MF}}[\boldsymbol{\rho}](t) \\ & + H_{\text{ph2}}^{\text{MF}}[\boldsymbol{\rho}](t) + \hat{H}_{\text{ex}}(t). \end{aligned} \quad (23)$$

The time evolution of an observable $\hat{\mathcal{O}}_S$ in the Schrödinger picture is described by $\hat{\mathcal{O}}_H(t) = \hat{\mathcal{U}}^{\text{MF}}(t)^{\dagger} \hat{\mathcal{O}}_S \hat{\mathcal{U}}^{\text{MF}}(t)$ in the Heisenberg picture. The latter satisfies the Heisenberg equation, $i\partial_t \hat{\mathcal{O}}_H(t) = \mathcal{U}^{\text{MF}}(t)^{\dagger} [\mathcal{O}_S, \hat{H}_{\text{tot}}^{\text{MF}}] \mathcal{U}^{\text{MF}}(t)$. From the Heisenberg equation for $\hat{\mathcal{O}} = \hat{\boldsymbol{\rho}}, \hat{X}_i, \hat{X}_{i,2}$, we obtain the equations of motion of these quantities.

To be more concrete, in the following discussion, we assume that $\hat{H}_{\text{ex}}(t)$ consists of only electron operators. The equation of motion for $\boldsymbol{\rho}(t)$ becomes

$$\partial_t \boldsymbol{\rho}(t) = i[\boldsymbol{\rho}(t), \mathbf{h}_{\text{el,tot}}^{\text{MF}}[\boldsymbol{\rho}, X, X_2](t)], \quad (24)$$

where $\mathbf{h}_{\text{el,tot}}^{\text{MF}}(t)$ is determined from $\hat{H}_{\text{el}}^{\text{MF}}(t) + \hat{H}_{\text{ex}}(t) = \sum_{i,a,j,b} \hat{c}_{ia}^{\dagger} [\mathbf{h}_{\text{el,tot}}^{\text{MF}}(t)]_{ia,jb} \hat{c}_{jb}$. For the type 1 phonons, we obtain

$$\partial_t X_i(t) = \omega_0 P_i(t), \quad (25a)$$

$$\partial_t P_i(t) = -\omega_0 X_i(t) - 2g \sum_a \rho_{i\bar{a},ia}(t), \quad (25b)$$

while for the type 2 phonons, we obtain

$$\partial_t X_{i,2}(t) = \omega_2 P_{i,2}(t), \quad (26a)$$

$$\partial_t P_{i,2}(t) = -\omega_2 X_{i,2}(t) - 2g_2 \sum_a (-)^a \rho_{i\bar{a},ia}(t). \quad (26b)$$

Equations (24), (25) and (26) form a closed set of differential equations for $\boldsymbol{\rho}(t)$, $X(t)$ and $X_2(t)$. We implement these equations in real space with the 4th order Runge-Kutta method. By choosing a spatially inhomogeneous $\hat{H}_{\text{ex}}(t)$ one can investigate the real-space propagation of the induced perturbation.

3. Linear response functions

In this section we discuss the expressions for the linear response functions evaluated by the tdMF theory introduced above. In particular, we are interested in the linear

response functions

$$\chi_{\mu\nu}^R(t-t'; \mathbf{r}_{ij}) \equiv -i\theta(t-t')\langle [\hat{\rho}_{\mu,i}(t), \hat{\rho}_{\nu,j}(t')] \rangle. \quad (27)$$

Here we used the fact that the linear response is translationally invariant in time and space, since the system is in equilibrium and translationally invariant without the external perturbation. We excite the system with a small perturbation of the form $\hat{H}_{\text{ex}}(t) = \delta F_{\text{ex},\nu j}^{\text{el}}(t)\hat{\rho}_{\nu,j}$ and measure the evolution of the order parameter $\hat{\rho}_{\mu,i}$. Since we take the order parameter ϕ to be real, χ_{11}^R corresponds to the dynamics in the amplitude direction, while χ_{22}^R corresponds to the dynamics in the phase direction. We also introduce the Fourier transformation of χ^R as $\chi^R(\omega; \mathbf{q}) \equiv \sum_l \int dt \chi^R(t; \mathbf{r}_l) e^{i\omega t - i\mathbf{q} \cdot \mathbf{r}_l}$.

The expression of the linear response function consistent with the tdMF is

$$\chi^R(\omega; \mathbf{q}) = \chi_0^R(\omega; \mathbf{q}) + \chi_0^R(\omega; \mathbf{q}) \Theta(\omega; \mathbf{q}) \chi^R(\omega; \mathbf{q}), \quad (28a)$$

$$\Theta(\omega; \mathbf{q}) = \begin{bmatrix} \frac{U}{2} & 0 & 0 & 0 \\ 0 & -\frac{U}{2} + g^2 D_0^R(\omega; \mathbf{q}) & 0 & 0 \\ 0 & 0 & -\frac{U}{2} & 0 \\ 0 & 0 & 0 & -\frac{U}{2} + g^2 D_2^R(\omega; \mathbf{q}) \end{bmatrix}.$$

Here, χ^R is a 4×4 matrix and consists of $\chi_{\mu\nu}^R$ with $\mu, \nu = 0, 1, 2, 3$. χ_0^R is the response evaluated by keeping the MF Hamiltonian the same as in equilibrium (without updating the MF parameters in the time evolution). In terms of Feynman diagrams, this corresponds to the bubble diagram and the concrete expression is

$$\chi_{0,\mu\nu}^R(\omega; \mathbf{q}) = \frac{1}{N} \sum_{\mathbf{k}} \left\{ \sum_{a,b=\pm} \text{Tr}[\hat{W}_a(\mathbf{k}-\mathbf{q}) \hat{\sigma}_\mu \hat{W}_b(\mathbf{k}) \hat{\sigma}_\nu] \times \frac{f(E_a(\mathbf{k}-\mathbf{q}), T) - f(E_b(\mathbf{k}), T)}{\omega - (E_b(\mathbf{k}) - E_a(\mathbf{k}-\mathbf{q})) + i\eta} \right\}, \quad (29)$$

where

$$\hat{W}_\pm(\mathbf{k}) = \frac{1}{2} \left[\pm \frac{B_{\mathbf{k}}^x}{B_{\mathbf{k}}} \hat{\sigma}_1 \pm \frac{B_{\mathbf{k}}^z}{B_{\mathbf{k}}} \hat{\sigma}_3 + \hat{\sigma}_0 \right]. \quad (30)$$

D_0^R and D_2^R are the free phonon Green's functions, $D_0^R(\omega; \mathbf{q}) = \frac{2\omega_0}{(\omega + i0^+)^2 - \omega_0^2}$, and $D_2^R(\omega; \mathbf{q}) = \frac{2\omega_2}{(\omega + i0^+)^2 - \omega_2^2}$. A detailed derivation of the susceptibilities is provided in [44].

B. Additional Results

In this section, we show additional theoretical results for the collective modes in the EI phase coupled to phonons at $T = 0$. In Sec. VIIB1 and Sec. VIIB2, we discuss the nature of the linear response functions and collective modes. In addition, we demonstrate the real space propagation after a local excitation. Here, we study a one-dimensional setup for which the real space simulation becomes simpler. In Sec. VIIB3, we discuss the anisotropy in the phase mode velocity by consider-

ing a two-dimensional setup with anisotropic hopping parameters. In particular, we show that the anisotropy is reduced close the BEC side.

1. Type 1 phonon

Here, we discuss the system with a single phonon mode of type 1, and set $\lambda_2 = 0$. We consider the one-dimensional setup and take $U_{\text{ref}} = 0.84$ eV, $J_1 = -J_0 = 0.4$ eV, $D_{01,\text{ref}} = 0.88$ eV, motivated by [48]. The phonon frequency is fixed to $\omega_0 = 0.08$ eV for numerical simplicity. This value is much larger than $1 \sim 3$ THz, and therefore the momentum where the phase mode and the phonon mode cross each other (q_0) becomes larger in the present analysis by a factor of about $10 \sim 20$ compared to the case with $\omega_0 = 1 \sim 3$ THz. As a result, the spot size needed to excite the mixed mode around q_0 becomes smaller by a factor of $10 - 20$. In the following we use the lattice constant $a = 0.35$ nm [29, 49] to convert the simulation results to SI units. While we use a larger phonon frequency than the experimental value of $1 \sim 3$ THz, this choice should only affect the quantitative dynamics, while qualitative arguments should remain robust. In the following calculation, the temperature is set to 100[K], which is well below the transition temperature. We note that Figs. 4 (A-F) in the main text are corresponding to Figs. S7(a)(c), Fig. S8(b) and Fig. S9, respectively.

In Fig. S7, we show the imaginary parts of the response functions χ_{11}^R and χ_{22}^R . When $\lambda = 0.0$, the phase mode is massless, and it exhibits a linear dispersion around $q = 0$, see Figs. S7(a) and S7(d). The corresponding velocity becomes $1.0 \times 10^5 \frac{\text{m}}{\text{s}}$, which is comparable to electronic velocities. The spectral weight of the phase mode is zero in χ_{11}^R at $q = 0$. While it shows some weight at finite q , this weight is much smaller than that of χ_{22}^R . This indicates that at finite q , there is mixing between the motions in the amplitude and the phase directions. In χ_{11}^R , a flat band appears around the band gap $\omega = 0.32$ eV, which correspond to the amplitude mode (analogous to the Higgs mode in the superconducting state). For non-zero el-ph coupling, the phase mode acquires a mass and a gap (Δ_{phase}) is opened. The massive phase mode starts to appear in χ_{11}^R even at $q = 0$, see Figs. S7(b) and S7(e). When the gap is small (the el-ph coupling is small), a crossing between the phonon mode and the massive phase mode occurs at nonzero \mathbf{q} . One can see the effect of hybridization in Figs. S7(b) and S7(e). As the el-ph coupling is increased the gap becomes larger [Figs. S7(c) and S7(f)], but hybridization occurs as long as the gap is still comparable to the phonon frequency. However, when the el-ph coupling becomes sufficiently strong, there is no clear hybridization between the massive phase mode and the phonon mode.

Now we demonstrate how these collective modes appear in the real space propagation. Before we show the results, we need to point out several issues. First, if we excite the system with optical frequencies, quasi-particles

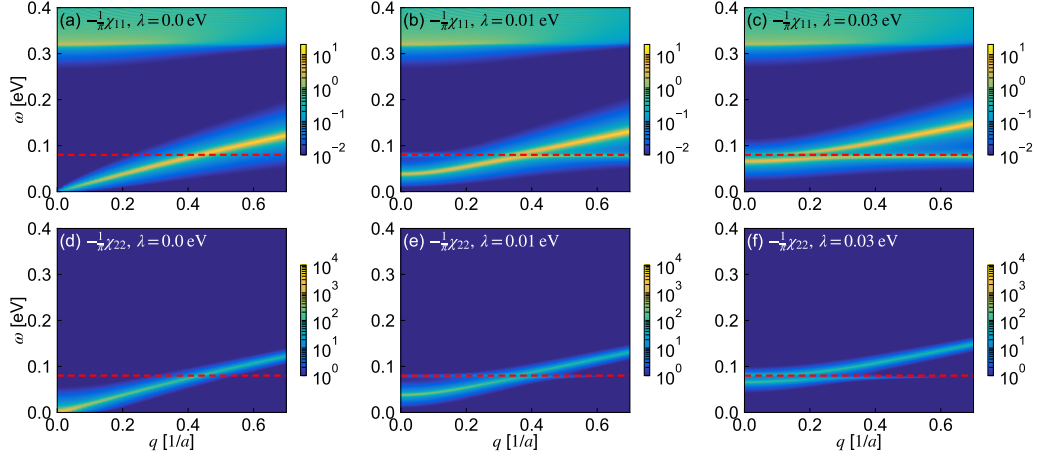


Figure S7. (First row) Imaginary part of the order parameter response function in the amplitude direction $-\frac{1}{\pi}\text{Im}\chi_{11}^R(\omega; q)$ for different electron-phonon couplings, namely (a) $\lambda = 0.0$ eV, (b) $\lambda = 0.01$ eV and (c) $\lambda = 0.03$ eV. (Second row) Imaginary part of the order parameter response function in the phase direction $-\frac{1}{\pi}\text{Im}\chi_{22}^R(\omega; q)$ for different electron-phonon couplings, namely (d) $\lambda = 0.0$ eV, (e) $\lambda = 0.01$ eV and (f) $\lambda = 0.03$ eV. The red dashed lines indicate the bare phonon frequency $\omega_0 = 0.08$ eV. Here, we use $U_{\text{ref}} = 0.84$ eV, $D_{01, \text{ref}} = 0.88$ eV and $\lambda_2 = 0.0$ eV. The panels (a) and (c) are identical to Fig4. (A) and (B) in the main text, respectively.

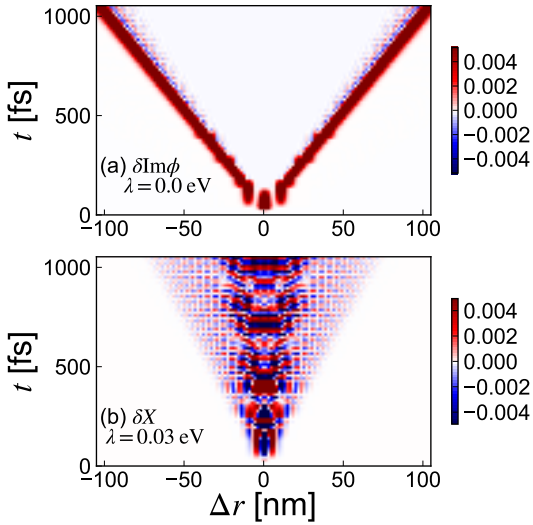


Figure S8. (a) Change in the imaginary part of the order parameter from its equilibrium value, $\delta\text{Im}\phi$, as a function of the distance from the center ($\Delta r \equiv r - r_0$) and time for the excitation at the center of the pure EI. (b) Change in the phonon displacement (δX) as a function of Δr and t for the excitation at the center of the el-ph coupled system. In both cases, the excitation parameters are $t_0 = 32.9$ fs, $\sigma_t = 6.6$ fs, $\delta D = 0.01$ eV, $\sigma_r = 1.8$ nm, $\Omega = 0.1$ eV. In panel (a) we use $U = 0.84$ eV, $D_{01} = 0.88$ eV, $\lambda = 0.0$ eV, and in panel (b) we use $U_{\text{ref}} = 0.84$ eV, $D_{01, \text{ref}} = 0.88$ eV, $\lambda = 0.03$ eV and $\omega_0 = 0.08$ eV. Panel (b) is identical to Fig. 4 (C) in the main text.

(QPs) as well as the phase mode are excited. Within the mean-field theory, both the QPs and the phase modes are ballistic and they can propagate to long-distances and for

a long time. However, in practice the QPs at high energies would be easily scattered by the lattice, disorder, or collisions with each other. Indeed, in Sec. IX we study the effects of disorder on both the QP and phase modes, and find that QP are always rapidly scattered by the disorder. By contrast, low-energy phase modes are robust against the disorder and can propagate ballistically on much longer length scales. Therefore, the response far from the excitation spot should be dominated by low-lying phase modes, and their dynamics will be our focus. As we will study their effect far from the excitation region, where diffusive QPs have yet to reach, the physical process by which the phase modes are excited is of lesser relevance. For these reasons, we do not excite the system by optical frequencies. Instead, we take into account the effect of the excitations as follows. A strong excitation at the center of the system can change the system parameters through nonlinear processes. Such a change would be much faster than the time-scale of the collective mode and phonons. Because nonlinear processes allow to excite modes with higher momenta, the size of the spot where the parameters are modulated is effectively reduced. This argumentation is consistent with the nonlinear pump-fluence dependence of the propagation length for the 2.9 THz phonon in the experiment.

As an example, we study the effect of a small change in the band-energy splitting between the two bands by modifying D_{01} and show how the mixed modes can propagate after the excitation at the center of the system. We note that such a modulation can be induced due to the change of the number of electrons in the conduction band and the valence band through the Hartree shift [42]. The

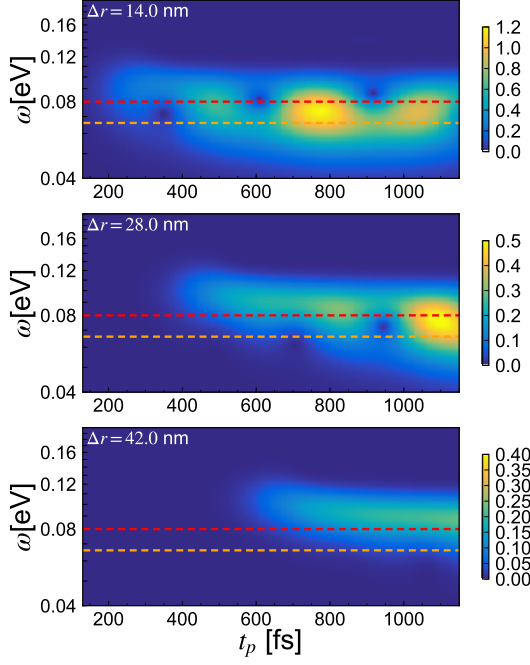


Figure S9. The windowed Fourier transformation of the phonon displacement $|\delta X(\omega, \Delta r; t_p)|$ is shown for specified Δr . The parameter set and the excitation conditions are the same as in Fig. S8(b). Here, we use $\sigma = 52.6$ [fs] for F_{Gauss} in Eq. (31). The orange dashed line indicates the gap of the phase mode, while the red dashed line indicates the bare phonon frequency. These results are identical to Fig 4 D,E,F in the main text.

explicit form of the excitation is

$$\hat{H}_{\text{ex}}(t) = \frac{\delta D}{2} \sum_i e^{-\frac{(t-t_0)^2}{2\sigma_t^2}} e^{-\frac{(r_i-r_0)^2}{2\sigma_r^2}} \cos(\Omega(t-t_0)) \hat{\rho}_{3i}.$$

In Fig. S8(a), we show the propagation for the pure EI phase. After the excitation at the center (r_0 indicates the center), the signal propagates with a velocity of around $1.0 \times 10^5 \frac{\text{m}}{\text{s}}$, which is the velocity of the massless phase mode. In Fig. S8(b), we show the propagation for nonzero el-ph coupling ($\lambda = 0.03$ eV). One can see that the signal is more involved than in the pure EI phase, but the front of the signal propagates with a velocity comparable to the massless phase mode for $\lambda = 0.0$ eV (for the present excitation $0.6 \times 10^5 \frac{\text{m}}{\text{s}}$ is observed). The propagating signal indeed involves the frequency of the phonon modes, which is clarified by the windowed Fourier transformation

$$\mathcal{O}(\omega; t_p) = \int dt e^{i\omega t} \mathcal{O}(t) F_{\text{Gauss}}(t - t_p), \quad (31)$$

where $\mathcal{O}(t)$ is some observable and $F_{\text{Gauss}}(t) = \exp(-\frac{t^2}{2\sigma^2})$. In Fig. S9, we show the windowed Fourier transformation of the difference in the phonon displacements from its equilibrium value $\delta X(t, \Delta r) = X(t, \Delta r) -$

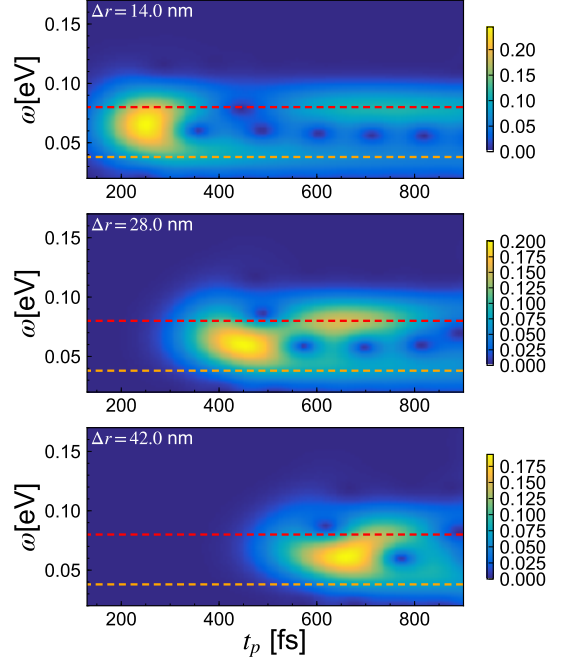


Figure S10. Same as Fig. 9, but with $\lambda = 0.01$ eV.

$X(0, \Delta r)$ for the specified positions. Here, $\Delta r \equiv r - r_0$. These results illustrate the propagation of the phonon mode and confirm that the fast propagation pointed out in Fig. S8 involves the phonon frequency. We note that the signals are beating with some frequency [see also Fig. S10]. This frequency roughly corresponds to the energy difference between the gap of the phase mode and the phonon, and it originates from the size of the window of the Fourier transformation. When we increase σ (increase the frequency resolution), the beating signals become less prominent.

In the above analysis, the gap of the phase mode is close to the phonon frequency [see Fig. S7(c)(f)]. Now, we show the results for another el-ph coupling ($\lambda = 0.01$) in Fig. S10 [see Fig. S7(b)(e)], where the gap is smaller than and well separated from the phonon frequency. Now, we can clearly observe the signal at Δ_{phase} and ω_0 as is predicted by the classical model of two coupled modes [see Sec. VI]. Thus, in principle, the results of the pump-probe experiment can include a signal at an energy corresponding to the gap of the phase mode, Δ_{phase} , although it is hard to tell where it is located and how to distinguish it from the phonon modes.

Finally, we need to note again that, in this simulation, we use a much smaller value for the range of the excitation compared to the experiment. This is because i) we use a much higher phonon frequency in the simulation, which makes the hybridization momentum larger, and ii) the velocity of the modes is of the same order but should be underestimated by a factor of 2-4, which additionally makes the hybridization momentum larger. Hence, in order to excite the mixing mode we need higher momen-

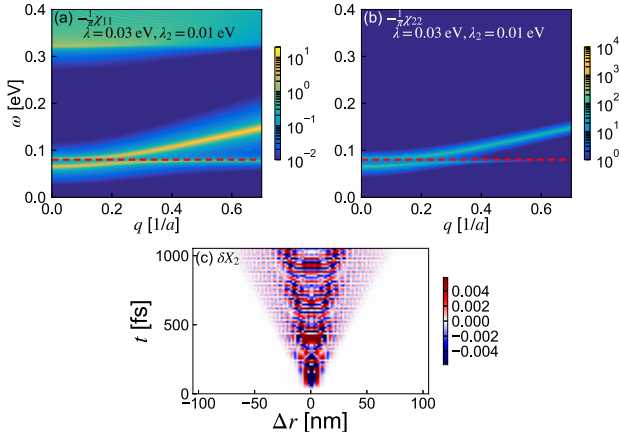


Figure S11. (a)(b) $-\frac{1}{\pi} \text{Im} \chi_{11}^R(\omega)$ and $-\frac{1}{\pi} \text{Im} \chi_{22}^R(\omega)$ for $\lambda = 0.03$ eV, $\lambda_2 = 0.01$ eV, respectively. The red dashed lines indicate the bare phonon frequency ω_2 . (c) Difference in the phonon displacement (δX_2) as a function of Δr and t for the excitation at the center of the el-ph coupled system with $\lambda = 0.03$ eV, $\lambda_2 = 0.01$ eV. The excitation parameters are $t_0 = 32.9$ fs, $\sigma_t = 6.6$ fs, $\delta D = 0.01$ eV, $\sigma_r = 1.8$ nm. Here, we use $\omega_2 = 0.08$ eV and $\omega_0 = 10^{-5}$ eV.

tum components. We also note again that in the experiment, because of non-linear processes, the excitation can include higher momentum components than what is estimated by the shape of the intensity profile of the laser.

2. Type 2 phonon

Now, we consider the propagation of the type 2 phonon. This mode itself does not break the continuous symmetry, so that the phase mode remains massless. Still, it can hybridize with the phase mode at finite momenta and thus exhibit a fast propagation after the excitation. To demonstrate this, in this section, we consider the one-dimensional setup and take $U_{\text{ref}} = 0.84$ eV, $J_c = -J_f = 0.4$ eV and $D_{01,\text{ref}} = 0.88$ eV. The phonon frequency is fixed to $\omega_2 = 0.08$ eV. We also consider a nonzero el-ph coupling to the type 1 phonon to take into account the effects of some other terms that break the continuous symmetry. We choose a small frequency of this optical phonon, namely $\omega_0 = 10^{-5}$ eV, to avoid any direct interaction between the type 2 and 1 phonon via the energy-scale separation.

In Figs. S11(a)(b), we show the imaginary parts of the response functions, namely χ_{11}^R and χ_{22}^R . One can see that the type 2 phonon can indeed hybridize with the phase mode. The phase mode has a nonzero mass because of the finite coupling with the type 1 phonon. In Fig. S11(c) we show the propagation of the signal in the phonon displacement X_2 after the excitation at the center and, in Fig. S12, its windowed Fourier transformation for specified sites. Here the excitation protocol is the same as in the previous section. Due to the coupling between the type 2 phonon and the massive phase mode at nonzero

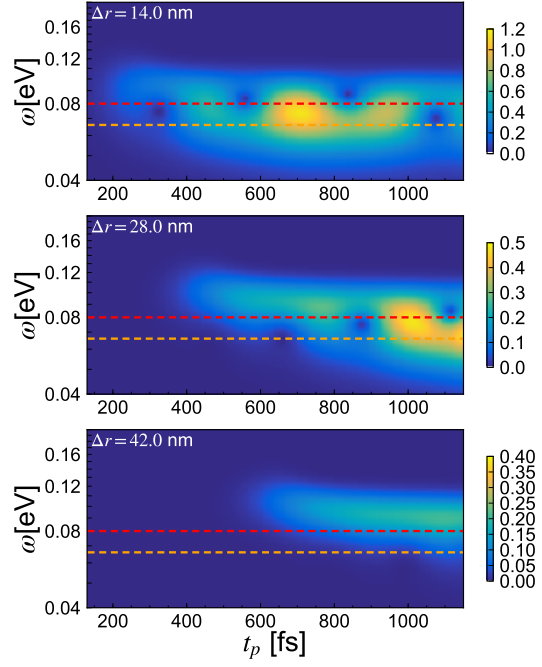


Figure S12. Windowed Fourier transformation of the phonon displacement $\delta X_2(\omega, \Delta r; t_p)$ are shown for specified Δr . The parameter set and the excitation conditions are the same as in Fig. S11(c). Here, we use $\sigma = 52.6$ [fs] for F_{Gauss} in Eq. (31).

momenta, the real-space results are similar to those in the previous section. This demonstrates that the type 2 phonon can also propagate fast because of the hybridization with the phase mode.

3. Anisotropy in the phase mode velocity

In this section, we discuss how the anisotropy in the velocity of the phase mode depends on the parameters when the hopping parameters show a large anisotropy. To study this, we consider a two-dimensional rectangular lattice with a strong anisotropy $J_1(\mathbf{a}_x) = -J_0(\mathbf{a}_x) = 0.4$ eV and $J_1(\mathbf{a}_y) = -J_0(\mathbf{a}_y) = 0.08$ eV, which is consistent with band structure calculations for TNS [50]. Here, \mathbf{a}_α indicates the lattice vector for the α direction. The x direction corresponds to the chain direction in TNS, while the y direction corresponds to the perpendicular direction of the chain. We set the lattice constant as $a_x = 0.35$ [nm] and $a_y = 0.7$ [nm] (we take into account that the y direction involves two sets of chains in one unit cell of TNS [50]). We focus on the pure EI and $T = 0$, and analyze how the velocity of the phase mode depends on the interaction U and the energy-level splitting D_{01} . We note that with increasing U and D_{01} the band splitting is also increased and the system approaches the normal semiconducting phase. Thus, the BEC regime corresponds to the regime of large U and large D_{01} . The velocities of the phase mode ($\omega(\mathbf{q})$) are evaluated for the α disper-

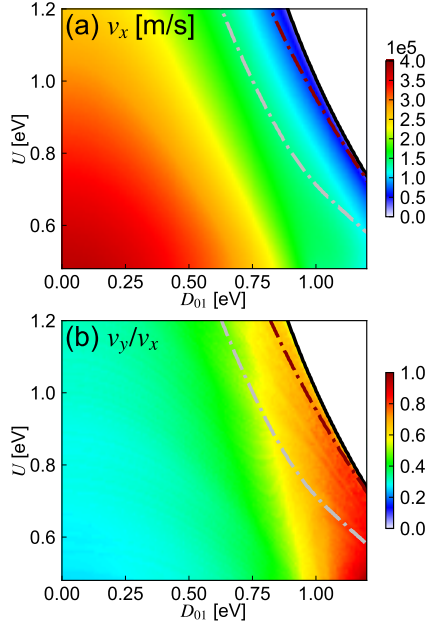


Figure S13. (a) Velocity of the phase mode along the x axis (v_x) and (b) the ratio between v_x and v_y . The velocities are obtained by a linear fit of the peaks in $-\text{Im}\chi_{22}^R(\omega, q_x, q_y)$. For v_x (v_y), we use $a_x q_x \in [0.05, 0.15]$ ($a_y q_y \in [0.05, 0.15]$) with $q_y = 0$ ($q_x = 0$). Black solid lines are the phase boundary between the normal semiconductor phase (above) and the EI phase (below). On the red dot-dashed lines, $B_{\mathbf{k}=0}^z$ in Eq. (20) is zero, so that the band structure without the EI order changes from the semiconductor-like bands to the semiconductor-like bands. Along the gray dot-dashed lines, the order parameter ϕ takes the maximum value as a function of U at each D_{01} . Roughly speaking, the BEC regime is above the gray line, while the BCS regime is below this line.

sion as $v_\alpha(\mathbf{q})|_{\mathbf{q}=0} = \frac{1}{\hbar} \frac{\partial \omega(\mathbf{q})}{\partial q_\alpha}|_{\mathbf{q}=0}$. In Fig. S13, we show v_x and the ratio v_y/v_x in the plane of U and D_{01} . The velocity is highest in the BCS regime, while the ratio v_y/v_x increases toward the BEC regime and it becomes close to one there. Although this is a rough estimation of the velocity of the phase mode, the small anisotropy of the propagation observed in the experiment is consistent with that the system is close to the BEC regime.

VIII. PHONON-POLARITON

In this section, we discuss what determines the spreading velocity of the phonon-polariton and which are the characteristic momenta for mixing between the phonon and photon degrees of freedom. We will first solve a model of coupled photons and phonons and then estimate corresponding quantities for Ta_2NiSe_5 . The coupled phonon-photon Hamiltonian can be written as a pair of harmonic oscillators [51]:

$$\hat{H}_{\text{coup}} = \sum_q \left[\frac{1}{2} \hat{\Pi}_{A,q}^\dagger \hat{\Pi}_{A,q} + \frac{1}{2} (\omega_{\text{ph}}(q)^2 + \omega_P^2) \hat{X}_{A,q} \hat{X}_{A,-q} + \frac{1}{2} \hat{\Pi}_{b,q}^\dagger \hat{\Pi}_{b,q} + \frac{\Omega^2}{2} \hat{X}_{b,q} \hat{X}_{b,-q} + \omega_P \hat{X}_{A,q} \hat{\Pi}_{b,-q} \right], \quad (32)$$

where X (Π) denotes the distortion (momentum) operator and their index A (b) the photon (phonon) degrees of freedom at momentum q . The first two terms correspond to the free photon problem with a dielectric term. The photon velocity is renormalized due to the dielectric function of the materials as $\omega_{\text{ph}}(q) = c_0 |q| / \sqrt{\epsilon}$, where c_0 is the velocity of the light in vacuum and ϵ is a dielectric function. We have introduced the phonon plasma frequency ω_P , which represents an effective light-matter coupling, and the transversal phonon frequency Ω . The last term includes an interaction between the two modes expressed with the displacement field.

We perform a unitary transformation $\hat{\Pi}'_{b,q} = \Omega \hat{X}_{b,q}$ and $\hat{X}'_{b,q} = -(1/\Omega) \hat{\Pi}_{b,q}$ so that the photon-phonon coupling is of the form $\Omega \omega_P \hat{X}_{A,q} \hat{X}'_{b,q}$. The Hamiltonian is

diagonal in the new momentum operators $\hat{\Pi}'_A$ and $\hat{\Pi}'_B$, while for the displacement operators it has the form

$$\hat{H} = \frac{1}{2} \sum_q [\hat{X}_A, \hat{X}'_B] \begin{bmatrix} \omega_{\text{ph}}^2 + \omega_P^2 & \omega_P \Omega \\ \omega_P \Omega & \Omega^2 \end{bmatrix} \begin{bmatrix} \hat{X}_A \\ \hat{X}'_B \end{bmatrix}. \quad (33)$$

We perform a Bogoliubov transformation using the unitary matrix $U_q = \begin{bmatrix} \cos(\phi_q) & \sin(\phi_q) \\ -\sin(\phi_q) & \cos(\phi_q) \end{bmatrix}$, where the coherence factors $\sin(\phi)$ ($\cos(\phi)$) determine the phonon (photon) character of the polariton. The diagonalization condition is $\tan(2\phi_q) = \frac{-2\omega_P \Omega}{\omega_{\text{ph}}(q)^2 + \omega_P^2 - \Omega^2}$ and we arrive at the polaritonic dispersion

$$\omega_{\pm}(q)^2 = \frac{1}{2} \left(\omega_{\text{ph}}(q)^2 + \omega_P^2 + \Omega^2 \pm \sqrt{[\omega_{\text{ph}}(q)^2 + \omega_P^2 + \Omega^2]^2 - 4\omega_{\text{ph}}(q)^2\Omega^2} \right). \quad (34)$$

From optical experiments on Ta_2NiSe_5 , see [52], we can estimate the upper limit for a dielectric function in the THz range as $\epsilon \leq 100$. This gives the upper limit for the propagation in the material, which is a tenth of the speed of light in vacuum, $3 \cdot 10^7$ m/s, and is much larger than the observed spreading velocity. Now, we consider a coupling to a 3 THz phonon mode, which is clearly seen in the experiment. A free parameter in the theory is the light-matter coupling given by the phonon plasma frequency ω_P , which we vary in Fig. S14. We will estimate the extreme case of the slowest possible light given in the ultra-strong coupling regime, where the photon plasma frequency equals the phonon frequency $\omega_P \approx \Omega$. While this regime is most probably unphysical, it may be considered as an extreme case scenario. As a measure of substantial mixing, we use $\cos(\phi) \approx 0.1$, see Fig. S14(b). This criterion yields the momentum $qa = 6 \cdot 10^{-4}$ that corresponds to the group velocity of $v = 1.6 \cdot 10^6$ m/s. This value is still an order of magnitude larger than the experimentally observed one despite taking the extreme limit. Therefore, we can safely claim that the polaritonic scenario is not consistent with the velocity observed in the experiment. We will estimate the extreme case of the slowest possible light given in the ultra-strong coupling regime, where the photon plasma frequency equals the phonon frequency $\omega_P \approx \Omega$. As a measure of substantial mixing, we use $\cos(\phi) \approx 0.1$, see Fig. S14(b). This criterion yields the momentum $qa = 6 \cdot 10^{-4}$ and the slowest group velocity is given by the lower polariton leading to $v = 1.6 \cdot 10^6$ m/s. This value is still an order of magnitude larger than the experimentally observed one despite the extreme limit. Moreover, the characteristic momentum where the photon and the phonon dispersions cross is given by $qa = 2.2 \cdot 10^{-4}$, see Fig. S14(a), which corresponds to $q = 6.3 \cdot 10^3 \text{ cm}^{-1}$ in TNS. This value is much smaller than the relevant momentum of the excitation estimated from the spot size, which means that the whole range of momenta is excited by the pump pulse. Therefore, the propagation of the wavefront is expected to be of the order of the photon velocity. While the minimum group velocity of the phonon-polariton might be strongly reduced for a large light-matter coupling, it will only affect the dynamics of the slower propagating modes and not the wavefront. In conclusion, we can safely claim that the polaritonic scenario is not consistent with the velocity observed in the experiment.

We should comment that the crossing condition $qa = 2.2 \cdot 10^{-4}$ corresponds to a spatial structure of size $L \approx 10 \mu\text{m}$, which is much larger than the experimentally observed disturbance. Despite the large structure, the disturbance spreading with the group velocity could still

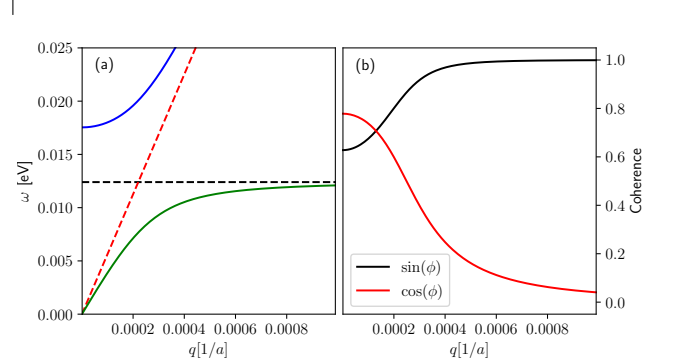


Figure S14. (a) Dispersion of a free 3 THz phonon (black dashed) and a free photon with $\epsilon = 100$ (red dashed). The full lines correspond to the phonon-polariton dispersion in the ultra-strong coupling regime $\omega_P = 3$ THz (full-lines). (b) Coherence factors corresponding to the strongly coupled phonon-polariton $\omega_P = \Omega = 3$ THz.

be observed.

IX. DISORDER SCATTERING

Here, we briefly outline the effects of introducing a disorder potential to model (12). Here, we focus on $\lambda = \lambda_2 = 0$ for simplicity. We will demonstrate that in the long-wavelength limit, disorder potentials which respect to the condensate $U(1) \otimes U(1)$ symmetry scatter the collective phase mode only weakly. This implies much longer mean free paths for the phase mode compared to those of the quasiparticles (QPs). This motivates the neglect of QP transport as compared to the collective mode (CM) transport.

A. Formalism

We consider the addition to the Hamiltonian of a local disorder potential

$$\hat{H}_{\text{dis}} = \sum_{i,\lambda} V_{\lambda i} \hat{\rho}_{\lambda i} \quad (35)$$

to the model (12). The potential $V_{\lambda i}$ ($\lambda = 0, 1, 2, 3$) is assumed to be Gaussian distributed, with zero mean and translationally invariant covariance relations

$$\langle V_{\lambda i} V_{\lambda' j} \rangle = K_{\lambda\lambda', |i-j|}, \quad \langle V_{\lambda}(\mathbf{q}) V_{\lambda'}(-\mathbf{q}) \rangle = K_{\lambda\lambda'}(\mathbf{q}),$$

where $K_{\lambda\lambda'}(\mathbf{q})$ encodes spatial correlations.

We distinguish between scattering channels $\lambda = 1, 2$

displacement signature to be carried ballistically to much further distances, thanks to the acquired electronic-scale velocity of the hybridized modes. This shows that it is

convenient to consider the phonons to be carried predominantly by the (ballistic) phase mode, without the QP excitations.